Journal Pre-proof

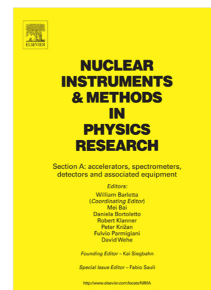

Silicon carbide diodes for neutron detection

José Coutinho, Vitor J.B. Torres, Ivana Capan, Tomislav Brodar, Zoran Ereš, Robert Bernat, Vladimir Radulović, Klemen Ambrožič, Luka Snoj, Željko Pastuović, Adam Sarbutt, Takeshi Ohshima, Yuichi Yamazaki, Takahiro Makino

PII: S0168-9002(20)31190-6
DOI: https://doi.org/10.1016/j.nima.2020.164793
Reference: NIMA 164793

To appear in: *Nuclear Inst. and Methods in Physics Research, A*

Received date : 10 July 2020
Revised date : 27 September 2020
Accepted date : 13 October 2020

Please cite this article as: J. Coutinho, V.J.B. Torres, I. Capan et al., Silicon carbide diodes for neutron detection, *Nuclear Inst. and Methods in Physics Research, A* (2020), doi: https://doi.org/10.1016/j.nima.2020.164793.

This is a PDF file of an article that has undergone enhancements after acceptance, such as the addition of a cover page and metadata, and formatting for readability, but it is not yet the definitive version of record. This version will undergo additional copyediting, typesetting and review before it is published in its final form, but we are providing this version to give early visibility of the article. Please note that, during the production process, errors may be discovered which could affect the content, and all legal disclaimers that apply to the journal pertain.

© 2020 Elsevier B.V. All rights reserved.

Manuscript
Journal Pre-proof
ed References

Silicon carbide diodes for neutron detection

José Coutinho[a,*], Vitor J. B. Torres[a], Ivana Capan[b], Tomislav Brodar[b], Zoran Ereš[b], Robert Bernat[b], Vladimir Radulović[c], Klemen Ambrožič[c], Luka Snoj[c,d], Željko Pastuović[e], Adam Sarbutt[e], Takeshi Ohshima[f], Yuichi Yamazaki[f], Takahiro Makino[f]

[a]*Department of Physics and I3N, University of Aveiro, 3810-193 Aveiro, Portugal*
[b]*Ruđer Bošković Institute, Bijenička 54, 10000 Zagreb, Croatia*
[c]*Jožef Stefan Institute, Jamova cesta 39, SI-1000 Ljubljana, Slovenia*
[d]*University of Ljubljana, Faculty of Mathematics and Physics, Jadranska cesta 19, 1000 Ljubljana, Slovenia*
[e]*Australian Nuclear Science and Technology Organisation, 1 New Illawarra Rd., Lucas Heights, NSW 2234, Australia*
[f]*National Institutes for Quantum and Radiological Science and Technology, 1233 Watanuki, Takasaki Gunma 370-1292, Japan*

Abstract

In the last two decades we have assisted to a rush towards finding a ^{3}He-replacing technology capable of detecting neutrons emitted from fissile isotopes. The demand stems from applications like nuclear war-head screening or preventing illicit traffic of radiological materials. Semiconductor detectors stand among the stronger contenders, particularly those based on materials possessing a wide band gap like silicon carbide (SiC). We review the workings of SiC-based neutron detectors, along with several issues related to material properties, device fabrication and testing. The paper summarizes the experimental and theoretical work carried out within the E-SiCure project (*Engineering Silicon Carbide for Border and Port Security*), co-funded by the NATO Science for Peace and Security Programme. The main goal was the development of technologies to support the fabrication of radiation-hard silicon carbide detectors of special nuclear materials. Among the achievements, we have the development of successful Schottky barrier based detectors and the identification of the main carrier life-time-limiting defects in the SiC active areas, either already present in pristine devices or introduced upon exposure to radiation fields. The physical processes involved in neutron detec-

*Corresponding author
Email address: `jose.coutinho@ua.pt` (José Coutinho)

Journal Pre-proof

Journal Pre-proof

tion are described. Material properties as well as issues related to epitaxial growth and device fabrication are addressed. The presence of defects in as-grown material, as well as those introduced by ionizing radiation are reported. We finally describe several experiments carried out at the Jozef Stefan Institute TRIGA Mark II reactor (Ljubljana, Slovenia), where a set of SiC-based neutron detectors were tested, some of which being equipped with a thermal neutron converter layer. We show that despite the existence of large room for improvement, Schottky barrier diodes based on state-of-the-art 4*H*-SiC are closing the gap regarding the sensitivity offered by gas-based and that of semiconductor detectors.

Key words: Neutron detection, silicon carbide, radiation defects

Journal Pre-proof

Journal Pre-proof

1 ## 1. Introduction

2 In the last two decades, we have witnessed a growing demand for devices capa-
3 ble of detecting neutron sources. Such a development is mostly explained by a shift
4 of the end-usage, from niche (fundamental research or inspection of nuclear warhead
5 limitation treatises [1–3]) to societal applications such as screening cargo at borders to
6 prevent illicit traffic of radiological materials [4, 5].

7 Considering the limited stock of ^{3}He available on Earth, semiconductor-based de-
8 tectors spring up as a strong alternative with many advantages, particularly in terms of
9 miniaturization and low operation bias, production yield and excellent gamma discrim-
10 ination. Silicon carbide (SiC) is nowadays an established semiconductor sustaining a
11 mature and growing industry of power electronics [6–8]. The motivation for leaving
12 behind the traditional silicon technology emanates from a strong demand for devices
13 with far greater power density, reliability, and overall performance (including cost).
14 All of these are specifications that only a wide band-gap semiconductor like SiC with
15 a large breakdown field, as well as exceptional thermal and mechanical stability, can
16 offer.

17 Silicon carbide, in particular the electronic-grade 4*H* hexagonal phase (4*H*-SiC)
18 [9, 10], has been proposed to be used for the fabrication of semiconductor-based ioniz-
19 ing radiation detectors [11–13], including neutrons [14–17]. SiC-based detectors com-
20 bine extreme radiation hardness with low leakage current, high signal to noise ratio,
21 and excellent neutron/gamma discrimination for pulsed radiation, thus being a strong
22 candidate to be used for particle detection under harsh conditions, including at high
23 temperatures and radiation [18].

24 Besides SiC, diamond is also a strong contender for the fabrication of solid-state
25 neutron detectors. Important advances in chemical vapor deposition (CVD) techniques,
26 allowed the successful fabrication of synthetic-diamond neutron sensors [19–22]. The
27 advantages of diamond stem primarily from its large atomic displacement threshold
28 energy (40-50 eV), which is substantially larger than that of SiC (20-35 eV). This
29 property potentially makes diamond more radiation tolerant.

30 A comparison between the performance of diamond and SiC devices for neutron

Journal Pre-proof

Journal Pre-proof

31 detection has been reported [17, 23, 24]. For thermal neutrons, single crystal CVD di-
32 amond devices showed better neutron-gamma discrimination, although as pointed out
33 by the authors, that was much owed to the use of a more effective thermal neutron con-
34 version layer in the diamond structures, which led to a higher energy deposition within
35 the detection volume [24]. Despite the larger atomic displacement threshold, diamond
36 detectors showed *polarization* effects for neutron fluxes above 10^9 n cm^{-2} s^{-1}. Polar-
37 ization of the structures arises from the creation of defects, where trapping/detrapping
38 of carriers takes place, inducing transient space-charge fields which interfere with the
39 signal from the ionizing radiation [21].

40 As for fast neutrons, both diamond and 4H-SiC detectors produced well character-
41 ized pulse high spectra with a well resolved $^{12}\mathrm{C}(\mathrm{n},\alpha)^{9}\mathrm{Be}$ peak. The larger detection
42 volume of the diamond device (with a capacitor structure) conferred a higher count rate
43 than the SiC device [17].

44 A typical SiC-based detector has a structure of a Schottky barrier diode (SBD), like
45 the one shown in Figure 1. Due to band alignment, a volume depleted of carriers is cre-
46 ated at the semiconductor side of the junction, making the device very sensitive to the
47 presence of electron-hole pairs generated upon illumination with above band-gap light
48 or upon exposure to ionizing radiation. Since neutrons do not interact with valence
49 electrons, their presence is deduced from detection of ionizing neutron reaction prod-
50 ucts, like gamma rays, alpha particles, tritons and larger ions. The device is operated
51 under reverse bias, which increases the potential drop across the semiconductor and
52 increases the depletion width. To limit the required operation voltage, the doping level
53 of the substrate is usually two orders of magnitude higher than that of the epi-layer.
54 Detailed specifications of SiC SBD detectors have been reported elsewhere by several
55 authors using n-n^+ structures [13, 14, 25, 26]. Although more difficult to fabricate,
56 p-n structures were also reported by Issa et al. [27].

57 The most probable interactions involving a fast neutron (E_n > 10 MeV) imping-
58 ing a SiC crystal involve elastic and inelastic recoil scattering events, $^{12}\mathrm{C}(\mathrm{n},\mathrm{n}')^{12}\mathrm{C}$
59 or $^{28}\mathrm{Si}(\mathrm{n},\mathrm{n}')^{28}\mathrm{Si}$ [28, 29], where some of the energy and momentum of the incident
60 neutron is transferred to C and Si nuclei. If the hit is strong enough to knock out a
61 crystalline atom from its site, the event can be recorded either as the permanent signa-

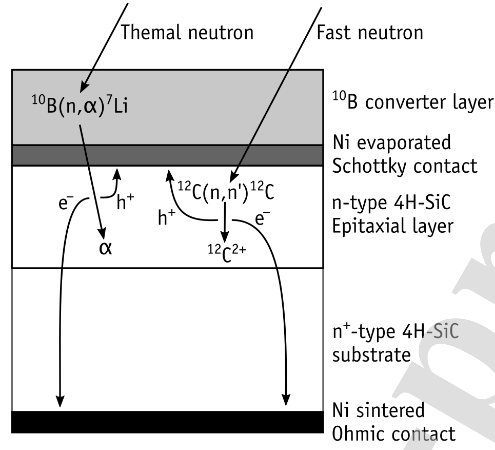

Figure 1: Design of a SiC Schottky barrier diode suitable for neutron detection. A converter layer covering the front contact is optional, and can substantially enhance the detection sensitivity to thermal neutrons due to the presence of a nuclide (such as ^{10}B or ^{6}Li isotopes) with high thermal cross section for (n,α), (n,p), (n,t) or similar reaction.

ture of the point defect created, or as a heavy ion moving through the depleted region, creating electron-hole pairs along its wake. This is shown on the right-hand side of Figure 1, were $^{12}\mathrm{C}^{2+}$ represents a recoil ion hit by a fast neutron. Depending on the neutron energy, detection of other ionizing products (*e.g.* from reactions $^{12}\mathrm{C(n, n')}3\alpha$ or $^{28}\mathrm{Si(n, n')}^{28}\mathrm{Al}$) is also possible [29].

The sensitivity of a fast neutron detector can be further improved by adding a converter material over the front contact [26]. It consists of a layer rich on a nucleus with large scattering cross-section for fast neutrons. The resulting recoil ions are responsible for the generation of electron-hole pairs within the depletion region of the SBD. Among the most effective converter materials are those with high density of hydrogen because of its high scattering reaction cross-section. Another advantage of hydrogenous fast neutron converters consists on the large recoil penetration depth of H^{+} into the semiconductor layer. Hydrogenous converter materials such as polyethylene show high conversion performance when compared to other materials [30]. Unfortunately, they usually cannot withstand high temperatures and/or harsh radiation environments.

Journal Pre-proof

Journal Pre-proof

78 Thermal and epithermal neutron detection can also be achieved via juxtaposition
79 of a converter layer rich in isotopes with large cross-section for neutrons with energy
80 in the range of $k_B T$ at room temperature (with k_B representing the Boltzmann con-
81 stant). Common choices are ^{6}Li, ^{10}B or ^{235}U. For a thermal neutron with kinetic en-
82 ergy E_n = 0.0253 eV (which corresponds to a velocity of 2200 m/s), their respective
83 absorption cross-section is σ_a = 938, 3843 and 681 barn, way much larger than 0.17
84 and 0.00353 barn for ^{28}Si and ^{12}C, respectively [31]. For ^{6}Li and ^{10}B the relevant re-
85 actions are respectively ^{6}Li(n, α)t and ^{10}B(n, α)^{7}Li. Figure 1 displays a possible device
86 architecture, where a ^{10}B-rich front layer is employed [27, 32]. While the ^{10}B cross
87 section is about four times that of ^{6}Li, it is important to note that the response of the
88 detector depends on other factors, including the penetration depth of the reaction prod-
89 ucts into the depletion region. In that respect the alphas and tritons emitted by ^{6}Li with
90 respective kinetic energy 2.05 MeV and 2.73 MeV, have the potential to generate more
91 excitations than the alphas and ^{7}Li^{+} ions with 1.47 MeV and 0.84 MeV that result from
92 the transmutation of ^{10}B [33].

93 Fission reactions involving ^{235}U split the uranium nucleus into two or exceptionally
94 three energetic fission fragments and give rise to the emission of secondary neutrons
95 and gamma radiation. Unfortunately, the interaction of heavy fission fragments with the
96 detection material is also responsible for considerable damage inflicted on the device,
97 particularly for fluences above 10^{13} n/cm^{2}, dramatically decreasing the observed count
98 rate [15].

99 The characterization of crystalline defects, either produced during operation or
100 those already present in as-grown material, is of paramount importance. As pointed
101 out by several authors [34, 35], the presence of a small group of defects in the SiC ac-
102 tive layer can ultimately determine the detector performance. Defects perturb the crys-
103 talline periodicity by introducing potential wells where charge carriers can be trapped.
104 Weak perturbations induce shallow states, where electrons and holes spend little time
105 before being emitted back to the valence or conduction band. On the other hand, strong
106 perturbations produce deep states, from which carriers escape with more difficulty [36].
107 Shallow and deep states in SiC can hold carriers with binding energies of the order of
108 0.1 eV and 1 eV, respectively. The ability of a defect to trap a carrier is essentially

Journal Pre-proof

109 determined by its capture cross section, and eventually by the existence of a significant
110 capture barrier [37].

111 When a semiconductor contains trapping defects, *i.e.* locations that interact with a
112 flux of carriers via trapping and detrapping events, the collection of the charge produced
113 by the incident radiation is delayed and not fully accounted for during the signal inte-
114 gration time. Moreover, after trapping a carrier, defects may become strongly attractive
115 to carriers of opposite charge, eventually leading to recombination via multi-phonon
116 emission [37]. The consequence is the dissipation of the detector signal through heat-
117 ing. It is therefore clear that the characterization of defects in SiC, either present in as
118 grown material, introduced during technological processes, or those created by ioniz-
119 ing radiation, is a crucial step towards improving radiation hardness and performance
120 of SiC-based detectors.

121 The carrier life-time is an important property with direct impact on detection perfor-
122 mance [38]. One promising way to improve carrier life-time is to limit the presence of
123 recombination defects and impurities via defect engineering. Important breakthroughs
124 were achieved by the groups of Kimoto [39] and Svensson [40], who found that high-
125 temperature (~ 1200 °C) oxidation followed by removal of the oxide layer leaves a SiC
126 top-layer ~ 50 μm deep, with the life-time being improved by at least a factor of two
127 with respect to the as-grown figure. The authors proposed that self-interstitials, injected
128 into the SiC during oxidation, were able to annihilate carbon vacancies (V_C defects),
129 decreasing their concentration to a level below 10^{11} cm^{-3} [39, 40]. Carbon vacan-
130 cies are even present in state-of-the-art epitaxial 4H-SiC. The defect has a rather low
131 formation energy of 4.8 eV [41], forms during high-temperature annealing (without
132 irradiation), and it is the main life-time-limiting defect in electronic-grade SiC. Other
133 promising techniques to control the concentration of V_C defects include annealing of
134 SiC encapsulated in a carbon-rich pyrolyzed resist film [41, 42], or ion-implantation
135 [43–45].

136 Defects in SiC and particularly in 4H-SiC, have been extensively studied using sev-
137 eral techniques, among which we single out electron paramagnetic resonance (EPR),
138 photoluminescence (PL) and deep level transient spectroscopy (DLTS) [9, 10]. The
139 latter is particularly powerful regarding the assessment of the impact of defects on de-

Journal Pre-proof

140 tector performance. DLTS is a junction spectroscopy method which gives us access to
141 the depth of traps (with respect to the semiconductor band edges) and capture cross-
142 sections for carriers. Details about DLTS and related techniques such as Laplace-DLTS
143 (L-DLTS) have been extensively discussed elsewhere [36, 46, 47].

144 Theory has also played a central role in the identification of defects in SiC [9, 48,
145 49], in particular electronic structure methods based on density functional theory [50].
146 Density functional software packages are common tools in modern laboratories, with
147 which one can simulate an electronic-scale picture of defects in solids, surfaces and
148 nanostructures [51, 52]. Many observables can be calculated and directly compared to
149 measured data, including *g*-tensors [53, 54], absorption and luminescence line shapes
150 [55], barriers and rates for thermally stimulated emission and capture of carriers [56],
151 vibrational spectra [57, 58], migration and reorientation [59, 60], stress-response of
152 spectroscopic signals [61], among many others.

153 The general requirements of neutron detectors for monitoring applications can be
154 divided into two main categories, the first related to the active components themselves
155 and the second related to the system implementation. In the first category we have the
156 detection efficiency (essentially the fraction of detected neutrons, usually expressed
157 as a percentage), background discrimination against gammas, response linearity, long-
158 term stability and radiation hardness. Requirements in the second category include
159 the temperature stability or operating temperature range, environmental factors like the
160 tolerance to mechanical shock, need for data acquisition/storage, maintenance, etc.

161 Requirements related to the active components can be addressed by the selection
162 of the underlying physics of detection (and subsequently by detector design, including
163 materials choice, optimizing geometry, or tailoring the acquisition system properties).
164 In this respect, it will be shown that carefully designed SiC detector prototypes can
165 offer high detection sensitivity, already matching current BF_3 detector technology [62],
166 and approaching ^{3}He detector technology. Additional specs offered are linear response
167 to the incident neutron flux and excellent degree of gamma discrimination (practically
168 100% sensitivity to neutrons) [63]. The later property is critical to isolate the neutron
169 signal from the often accompanying gamma and X-ray radiation fields. This is pos-
170 sible with materials like SiC and diamond thanks to the low atomic number of their

Journal Pre-proof

Journal Pre-proof

171 constituents [14, 23, 64]. It is also noted that neutron-gamma discrimination in SiC
172 SBD detectors can be tuned by changing the working bias [24].

173 Radiation hardness of SiC is also addressed in this review. It will be shown that
174 defects, *i.e.* radiation-induced degradation of the detectors, only occurs for epithermal
175 / fast neutron fluence levels of the order of 10^{11} n/cm^2 [65, 66], which is extremely high
176 in the context of border and port security monitoring. Macroscopic radiation hardness
177 or the long-term stability of these detectors are not covered.

178 Requirements related to the system implementation are addressed by design of
179 structural components (including housing, thermal insulation or temperature control,
180 mechanical isolation and damping) and the acquisition system. For border and port
181 monitoring it is advantageous if detectors and associated electronics are robust, simple
182 to operate/maintain, and operable in a wide temperature range. The mechanics of SiC
183 itself, being an extremely resistant ceramic being used in a variety of harsh applica-
184 tions, combined with the wide electronic bandgap and ability to be doped with both
185 n- and p-type dopants, are key advantages in view of these requirements. Regarding
186 the acquisition systems, for a single SiC-based detector they are very similar to those
187 of gas-based ionization detectors. However, in the context of border and port monitor-
188 ing, large arrays of SiC detectors would be needed, each detector registering a separate
189 signal, needing to be digitized, processed and combined. This presents a technologi-
190 cal challenge, which reminds us the complexity of detectors developed in the context
191 of high-energy physics experiments. However, this will be largely mitigated with the
192 rapid development of accessible, open source, low cost and highly complex electronics,
193 which are leveraging advances in a multitude of different fields, including nuclear and
194 aerospace.

195 In the following sections, we will describe a series of experiments and calculations
196 involved in the design, fabrication and characterization of 4*H*-SiC thermal neutron
197 detectors. We start Section 2 describing the properties of SiC materials. We proceed to
198 Section 3 where we detail the growth of the SiC layers and fabrication of the Schottky
199 junctions. In Section 4 we report on the characterization of the most harmful defects
200 present in as-grown and irradiated material. Particular attention is given to the V_C
201 defect. In Section 5 we describe a prototype detection system, followed by the results

Journal Pre-proof

202 from field-testing. Finally, conclusions and an outlook are drawn in Section 6.

203 2. SiC properties

204 Silicon carbide is perhaps the best example of a compound that shows polytypism.
205 This property consists on the formation of distinct polymorphs (different crystalline
206 structures with a common stoichiometry) coherently stacked along a crystalline direc-
207 tion. In SiC, the stacking occurs along the ⟨0001⟩ direction of the hexagonal close-
208 packed lattice. According to Figure 2(a), three possible sites are available, namely A,
209 B and C (shown as black, gray and white circles, respectively). The stacking is made
210 with ⟨0001⟩-aligned Si-C dimers, so that each atomic bilayer is of type A, B or C.
211 Although there are in principle infinite combinations of periodic stacking sequences,
212 only a few are grown with acceptable quality, namely (AB), (ABC), (ABCB) and (AB-
213 CACB). According to Ramsdell's notation [67], these polytypes are referred to as $2H$,
214 $3C$, $4H$ and $6H$, respectively, indicating the number of SiC bilayers per unit cell and
215 the lattice system (H - hexagonal, C - cubic, R - rhombohedral).

216

217 It is also common to distinguish Si-C dimers by their site-symmetry as perceivable
218 by the arrangement of their first neighbors [68]. For instance, the A,h-labeled Si-C
219 dimer of stacking type A at the bottom of Figure 2(b) has three Si and three C neigh-
220 bors whose locations are equivalent by symmetry with respect a (0001) mirror plane
221 crossing the Si-C bond.[1] In $2H$-SiC (*wurtzite* structure) all Si-C dimers show this ar-
222 rangement, and because of that they are labeled with an "h" (standing for hexagonal
223 site). The same happens with Si-C dimers of stacking type C in Figure 2(b). On the
224 other hand, Si-C dimers of stacking type B have neighbors whose sites do not map
225 to each other upon {0001} reflection. Instead, their neighboring sites transform with
226 inversion symmetry at the center of the bond. This is analogous to the case of cubic
227 $3C$-SiC (*zincblende* structure), where all Si-C bilayers show this arrangement. Hence,
228 in the case of hexagonal polytypes, these sites are labelled with the letter "k", which

[1] We are assuming an ideal crystalline structure with all atoms forming identical and perfect tetrahedral bonds with their neighbors.

Journal Pre-proof

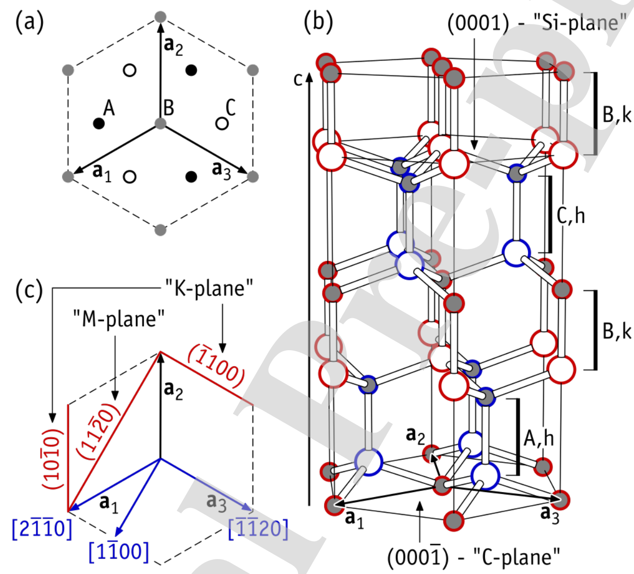

Figure 2: Crystalline properties of SiC. (a) Possible stacking sites (A, B or C) for Si-C dimers shown as black, gray and white circles, respectively. (b) Crystal structure of 4*H*-SiC illustrating the (ABCB) stacking sequence combined with the site-symmetry of atoms: pseudo-cubic (A,k and B,k) and hexagonal (A,h and B,h). Carbon and silicon atoms are colored gray and white, respectively. (c) High-symmetry crystallographic planes (within parentheses) and directions (within square brackets) using the four-index Miller-Bravais and Weber notations, respectively.

stands for cubic (or more appropriately pseudo-cubic, considering that the cubic-like symmetry is lost if we consider atomic shells beyond the first neighbors).

For the sake of reference, we also depict in Figure 2(c) a few high symmetry planes and directions using the four-index Miller-Bravais and Weber notations, respectively, which are commonly used for hexagonal crystal systems [69]. These can be related to the three-index Miller notation. The conversion of an (hkl) plane to the Miller-Bravais notation is straightforward, essentially involving the addition of a third basal index (which is linearly dependent on h and k),

$$(hkl) \equiv (hkil), \text{ with } h + k + i = 0. \tag{1}$$

Although being redundant, the index i makes index permutation symmetries more clear. For instance, as depicted in Figure 2(c), planes (1010) and (1100) are symmetrically equivalent, and that would not be apparent if they were represented within the Miller scheme as (100) and (110), respectively. For crystallographic directions, an analogous four-axes extension is available, known as Weber notation, where $[UVTW]$ relates to a three-index $[uvw]$ counterpart as

$$U = (2u - v)/3 \tag{2}$$
$$V = (2v - u)/3 \tag{3}$$
$$T = -(u + v)/3 \tag{4}$$
$$W = w, \tag{5}$$

where $U + V + T = 0$ is again verified, and the Weber indices of the direction perpendicular to a lattice plane are the same as the Bravais-Miller indices of that plane. Like in the Miller-Bravais notation for planes, the Weber notation exhibits all permutation symmetries among equivalent directions. This is shown in Figure 2(c), where the equivalence of $[2\bar{1}\bar{1}0]$ and $[\bar{1}\bar{1}20]$ is much more evident than if they were represented as $[100]$ and $[\bar{1}\bar{1}0]$, respectively.

We can think of all possible polytypes as ranging from $2H$ (purely hexagonal) up

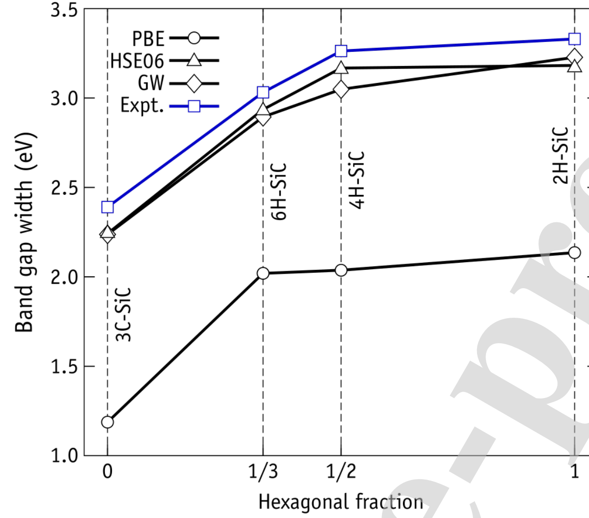

Figure 3: Variation of the band gap of SiC polytypes as a function of their hexagonal fraction. Both experimental (squares) and theoretical estimates within several approximations, namely the generalized gradient approximation (PBE), hybrid density functional approximation with screened exact exchange (HSE06), and many-body perturbation theory within *GW*, are shown.

251 to 3*C* (purely cubic), with other structures representing intermediate cases with partial
252 hexagonality. 4*H*- and 6*H*- for instance, have 1/2 and 1/3 fractions of hexagonal bi-
253 layers (per unit cell). Interestingly, the band gap width of SiC increases monotonically
254 with the hexagonality fraction [70]. At cryogenic temperatures, the experimental band
255 gap widths are E_g = 2.39 eV, 3.02 eV, 3.26 eV and 3.33 eV for 3*C*-, 6*H*-, 4*H*- and
256 2*H*-SiC, respectively [9, 71]. These values are plotted in Figure 3 (squares), along with
257 analogous quantities obtained from first-principles employing different approximations
258 to the exchange-correlation interactions between electrons. These include the gener-
259 alized gradient approximation (PBE, circles), hybrid density functional approximation
260 involving a mix of local and non-local screened exchange contributions (HSE06, tri-
261 angles), and many-body perturbation theory within the Greens function method with
262 screened potential (*GW*, diamonds).

263 Despite the relative offsets with respect to the observed E_g values, theory describes
264 rather well the variation with the hexagonal fraction. Although not currently clear, the

Journal Pre-proof

Journal Pre-proof

reasoning for such variation is possibly connected with an increase in the ionicity of the phases with higher hexagonal fraction due to an increase of the internal crystal field.

The E_g values obtained within the generalized gradient approximation (according the Perdew, Burke and Ernzerhof, PBE [72]) underestimate the experiments by about 50%. This is a well known insufficiency of this method, and it is mostly attributed to self-interaction errors. These effects are accounted for by many-body perturbation calculations [73] (*GW*, diamonds), which removes self-interactions in the electronic correlation, and that leads to E_g values already very close to the measured figures. We can also note from Figure 3 than the *GW* results invariably underestimate the experimental data by up to 0.2 eV. This is explained by the slightly over-delocalized one-electron states used, which were taken from a density functional calculation within the generalized gradient approximation.

Figure 3 also shows the band structure obtained using hybrid density functional theory. This method provides E_g values comparable to those obtained by *GW*. Essentially, hybrid density functional theory mixes a portion of exact exchange (in the spirit of the Hartree-Fock method) using the Kohn-Sham orbitals. Electron correlation interactions are still addressed using a local or semi-local method (such as PBE). Despite having to evaluate a four-center integral involving the Kohn-Sham orbitals, hybrid density functional methods are still much lighter than *GW*, which accounts for the many-body electron-electron interactions via screening of the exchange interactions using a frequency-dependent microscopic dielectric matrix.

The specific hybrid density functional employed, HSE06 (firstly proposed by Heyd, Scuseria, and Ernzerhof [74] and subsequently improved by Krukau *et al.* [75] in 2006), numerically screens the weak long-range exchange contributions, making the method more efficient and as accurate as *bare* hybrid functionals.

Figure 4 shows the first Brillouin zone for a hexagonal crystal, along with the electronic band structure of 4*H*-SiC calculated using many-body perturbation theory (*GW*) and hybrid density functional theory (HSE06). Importantly, both methods show quite similar band structure across the entire Brillouin zone. The origin of energy was set at the top of the valence band in both calculations. As already referred above, the differ-

Journal Pre-proof

Journal Pre-proof

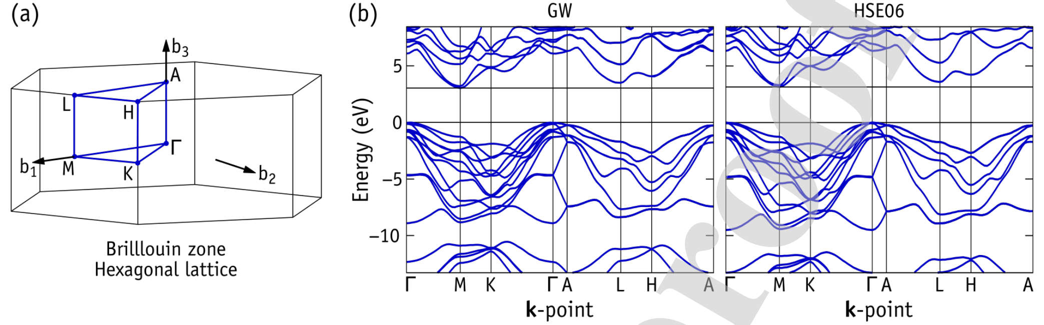

Figure 4: (a) First Brillouin zone of a hexagonal lattice along with reciprocal-space segments between several high-symmetry **k**-points. (b) Electronic band structure of 4*H*-SiC based on quasi-particle energies from many-body perturbation calculations (*GW*) and based on the Kohn-Sham energies from hybrid density functional calculations (HSE06).

296 ence between the band gap widths in both calculations is only 0.1 eV (E_g = 3.04 eV
297 and 3.17 eV from GW and HSE06 theory levels, respectively). The valence band top
298 and conduction band bottom states occur at $\mathbf{k} = \Gamma$ and $\mathbf{k} = M$ (along $\langle 2\bar{1}\bar{1}0 \rangle$ in re-
299 ciprocal space), respectively. The similarity of the results from both methods suggest
300 that electronic structure calculations of defects that introduce deep traps into SiC can
301 be accurately calculated using hybrid density functional methods [76].

302 We end this section with a summary of some physical properties of the most com-
303 mon SiC polytypes, which are reported in Table 1.

304

305 3. Material growth and device fabrication

306 Active layers of SiC electronic devices are grown over a wafer made of bulk mate-
307 rial which provides mechanical support. The most common method to grow bulk SiC
308 is seeded sublimation (also known as modified Lely method) [80]. Accordingly, SiC
309 powder is RF-heated in a graphite crucible to about 2500 °C, and upon sublimation,
310 Si_2C and SiC_2 molecules are deposited on a SiC seed crystal, which is located near the
311 lid of the crucible, and kept at a slightly lower temperature to promote condensation
312 (see Chapter 4 of Ref. 10 and references therein). Currently, several SiC manufacturers

Table 1: Some physical properties of SiC polytypes as function of their hexagonal fraction (HF): Lattice parameters at room temperature (for the sake of comparison with the hexagonal phases, a and c/a for 3C-SiC are reported considering $c/a = a_0\sqrt{2}/2$, where a_0 is the conventional cubic lattice parameter) [77], bulk modulus (B) [77], static dielectric constant (ϵ_0 values from the 6H-SiC polytype are normally used for 4H-SiC. For 2H-SiC only an orientationally average value is available) [77], electronic band gap width (E_g) [78], electron and hole mobility ($\mu_{e/h}$) [79], and breakdown field (E_B). A doping concentration of 10^{16} cm^{-3} is assumed when applicable.

Property	3C-SiC	6H-SiC	4H-SiC	2H-SiC
Space group	$F\bar{4}3m$	$P6_3mc$	$P6_3mc$	$P6_3mc$
HF	0	1/3	1/2	1
a (Å)	3.0827	3.0806	3.0798	3.0763
c/a	2.178	4.907	3.262	1.641
E_g (eV)	2.39	3.02	3.26	3.33
$\epsilon_{0,\perp}$	9.72	9.66		10.0
$\epsilon_{0,\parallel}$		10.03		
B (GPa)	230	230-234	217	223
$\mu_{e,\perp}$ (cm^2/Vs)	750	360	800	
$\mu_{e,\parallel}$ (cm^2/Vs)		97	880	
μ_h (cm^2/Vs)	40	90	115	
E_B (MV/cm)	~ 4	~ 3	~ 3	

Journal Pre-proof

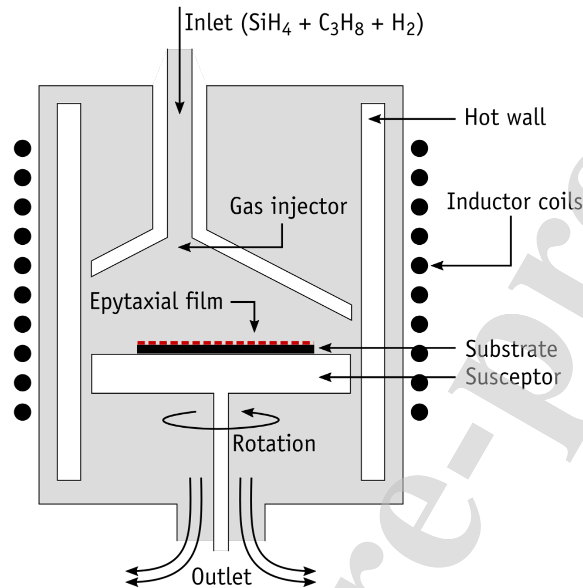

Figure 5: Schematic cross-section of a CVD reactor employed to grow epitaxial layers of SiC (adapted from Ref. 81).

313 supply single crystal wafers produced by seeded sublimation with a diameter as large
314 as 6-inch.

315 Active layers in devices are produced by means of homoepitaxial growth using
316 CVD, allowing polytype replication and both p- and n-type doping. This is achieved
317 by using the so called step-flow growth and by controlling the C/Si ratio, respectively.
318 Silane (SiH_4) and propane (C_3H_8) are common precursor gases, while hydrogen (H_2),
319 sometimes mixed with argon (Ar), is used as carrier gas. The typical growth temper-
320 ature is in the range 1600-1650 °C and the growth rate is around 100 μm/h (about 10
321 times slower than substrate growth by seeded sublimation). Developments in CVD
322 growth of SiC by Ito and co-workers [81] achieved simultaneous high growth rate (up
323 to 250 μm/h), large-area uniformity and doping homogeneity.

324

325 A schematic diagram of a CVD reactor is depicted in Figure 5. The design in-
326 corporates the essential features of the reactor used to grow the epi-SiC layers of the

Journal Pre-proof

Journal Pre-proof

327 Schottky diodes which will be described below. It comprises a vertical hot-wall reactor
328 with downward gas flow, with graphite walls heated by induction coils, while heating
329 of the rotating susceptor is achieved via internal radiation.

330 The reactor setup possesses a gas injector allowing reactants to be supplied directly
331 onto the substrate, thus helping to achieve high growth rates. An H_2-etching step pre-
332 ceding the actual growth is performed at about 1400 °C. The purpose of the *in-situ*
333 etching is two-fold, namely (i) pull off a few top layers of the substrate to remove
334 subsurface damage and (ii) obtain a regular stepped surface which is essential for the
335 replication of the underlying substrate polytype (thus the name step-controlled epitaxy)
336 [82]. The particular success of 4*H*-SiC homoepitaxy in terms of the resulting SBD
337 quality, paved its way to become the material of choice for power device applications.

338 A growth rate as high as 250 μm/h has been achieved at a SiH_4/H_2 ratio of 0.005
339 (C/Si ratio fixed to 1.0) [81]. For higher ratios (and consequently gas flow rates),
340 the epi-layer surface became rough due to formation of 3*C*-SiC domains. Large-area
341 uniformity has been optimized by allowing a lateral displacement of the gas injection
342 with respect to the center of the reactor (see Figure 5). This enhances the effect of the
343 susceptor rotation, and leads to uniform growth rates and doping concentration along
344 the radial direction of the substrate [81]. The resulting material shows good optical
345 and electrical specifications. Photoluminescence spectroscopy shows that free-exciton
346 recombination stands as the main radiative decay channel. On the other hand, DLTS
347 indicates the presence of three deep traps, the two most prominent (commonly referred
348 to as $Z_{1/2}$ and $EH_{6/7}$) occurring with a concentration below 10^{13} cm^{-3}.

349 The SiC detectors which will be reported in the sections below, consisted of Schot-
350 tky barrier diodes based on n-type 4*H*-SiC. A Schottky (rectifying) junction between
351 a metal and a n-type semiconductor is formed when the work function of the metal
352 exceeds the electron affinity of the semiconductor ($\phi_m > \chi_s$), while an Ohmic contact
353 is formed when ($\phi_m \leq \chi_s$). Because 4*H*-SiC has a relatively low electron affinity, most
354 metals form Schottky barriers. The barrier height is given by $\phi_B = \phi_m - \chi_s$ and depends
355 whether it is formed on the C-face or Si-face surface ($\phi_{B,C}$ or $\phi_{B,Si}$). For the case of
356 a Ni contact, these were measured as $e\phi_{B,C} = 1.87$ eV and $e\phi_{B,Si} = 1.69$ eV, respec-
357 tively [83]. Ohmic contacts on n-type 4*H*-SiC are often made by annealing a layer of

Journal Pre-proof

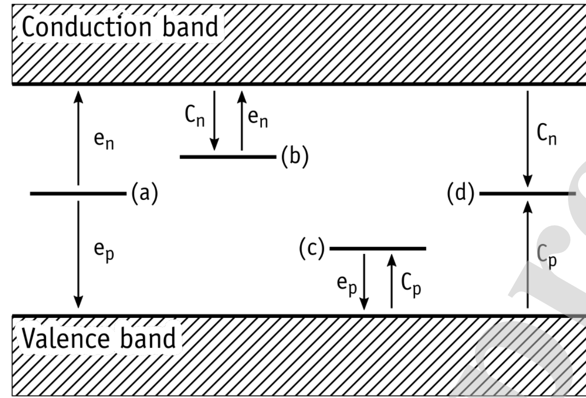

Figure 6: Diagram with defect states within the band gap representing (a) a generation process via a deep state in a depletion region, (b) electron trapping in n-type, (c) hole trapping in p-type, and (d) recombination of carriers. Symbols $e_{n/p}$ and $C_{n/p}$ denote emission and capture processes for electrons and holes (subscripted n and p, respectively).

358 the same metal used for the Schottky barrier. The thermal treatment has the effect of
359 creating a thin silicide with a reduced barrier height [84].

360 In the present work we used n-type silicon carbide SBDs, fabricated using nitrogen-
361 doped ([N] in the range (4.7-9.1) $\times$ 10^{14} cm^{-3}) 4H-SiC epi-layers with a thickness in
362 the range 25-170 μm, grown on n$^+$-type wafers. The Schottky barrier was formed
363 by evaporation of nickel through a metal mask with patterned squared apertures of
364 1 mm $\times$ 1 mm, while Ohmic contacts were formed by nickel sintering at 950 °C in Ar
365 atmosphere on the back side of the silicon carbide substrate [85].

366 4. Defect characterization

367 Depending on their affinity for electrons and holes, deep level defects can act as
368 trapping, recombination or generation centers. Deep level defects severely affect the
369 performance of devices and thus are followed with interest by the semiconductor scien-
370 tific and industrial communities. Their characterization is therefore crucial for future
371 improvement of the radiation hardness and extending the integrity of semiconductor
372 detectors.

373

Journal Pre-proof

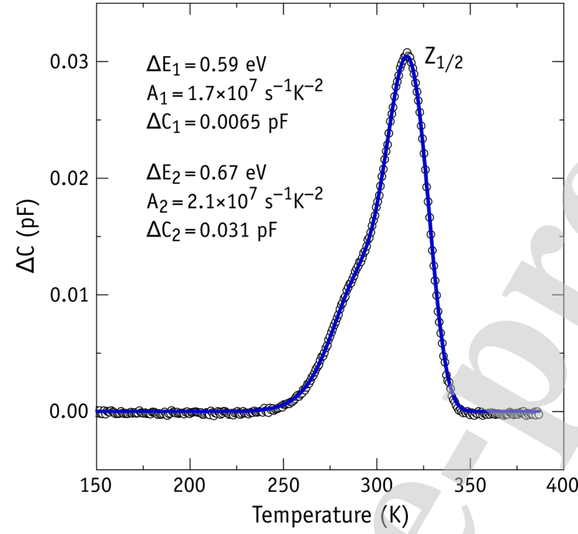

Figure 7: Conventional DLTS spectrum (data points) obtained for an as-grown n-type 4*H*-SiC SBD. Reverse bias, pulse voltage, and width were $V_\mathrm{r} = -10$ V, $V_\mathrm{p} = 0$ V, and $t_\mathrm{p} = 1$ ms, respectively. The solid line is the simulated DLTS spectrum. Reproduced from Ref. 86, with the permission of AIP Publishing.

374 The technique of choice for deep level defect characterization is DLTS. The method
375 has played a prominent role towards our understanding of electrically active defects in
376 semiconductors, combining high sensitivity with reasonable energy and spatial reso-
377 lution. In DLTS, a steady reverse voltage applied to a junction (Schottky or p-n) is
378 perturbed by a pulse bias, which has the effect of injecting majority carriers into the
379 space-charge volume thus filling available deep traps (provided that the filling pulse is
380 long enough). Upon removal of the pulse bias, majority carriers are emitted back to
381 the crystalline states and freed from the traps, thus restoring the width of the depletion
382 region. The realm of DLTS lies on following the rates of filling and emptying of the
383 defect traps by measuring the capacitance transients of the sample diode [36, 46].

384

385 Figure 6 represents the main carrier emission/capture events that can be measured
386 by DLTS. Analysis of the kinetics underpinning these processes is usually based on
387 Schokley-Read-Hall (SRH) statistics [37, 87]. For the case of an n-type semiconductor,
388 the rate of capture of a flux of electrons by a deep trap possessing a characteristic

Journal Pre-proof

389 electron capture cross-section σ_n is

$$C_n = \sigma_n \langle v_n \rangle n, \tag{6}$$

390 where n is the free-electron density traveling at an average thermal velocity $\langle v_n \rangle =$
391 $(3k_B T/m^*)^{1/2}$ and m^* is the free-electron effective mass. The capture cross section
392 describes a thermally-activated capture process [37] and has a temperature-dependence
393 of

$$\sigma_n(T) = \sigma_{n\infty} \exp(-\Delta E_\sigma / k_B T). \tag{7}$$

394 Equation 7 depends on the so called *direct capture cross-section* $\sigma_{n\infty}$ and capture bar-
395 rier ΔE_σ, and these quantities are usually measured by following the capture rate and
396 varying the duration of the filling puse [36]. It is noted that an analogous set of equa-
397 tions could be written for the capture of holes.

398 Immediately after the filling pulse, the diode becomes again reverse biased and
399 electron emission becomes dominant over capture. The rate of electron emission to the
400 conduction band is then

$$e_n = \sigma_{n\infty} g \langle v_n \rangle N_c \exp\left(-\Delta E_{na}/k_B T\right), \tag{8}$$

401 where g accounts for the degeneracy ratio between states before and after electron
402 emission, N_c is the effective density of states in the conduction band, and ΔE_{na} is an
403 activation energy for electron emission from the trap to the conduction band bottom.

404 The standard procedure of a DLTS measurement is to find the activation energy for
405 carrier emission (from a trap) performing a sequence of isothermal measurements at
406 different temperatures. This is done by monitoring the capacitance of the diode at the
407 selected temperature after filling the trap, which should vary as

$$\Delta C(t) = \Delta C_{max}\left[1 - \exp(-e_n t)\right], \tag{9}$$

408 and determining the emission rate e_n for that particular temperature. Because the $\langle v_n \rangle N_c$
409 product has a T^2-dependence, DLTS emission data is usually cast as a log plot of e_n/T^2

Journal Pre-proof

410 against $1/k_BT$, and therefore ready to be fitted against an Arrhenius straight line. From
411 the fit, the intercept of the plot with the $\log(e_n/T^2)$-axis at $1/k_BT = 0$ is identified as the
412 apparent capture cross section, whereas the slope is the activation energy for electron
413 emission, $\Delta E_{na} = \Delta E_t + \Delta E_\sigma$, allowing us to extract ΔE_t, *i.e.* the actual location of
414 the trap with respect to the conduction band minimum [36, 37, 47]. It is noted that due
415 to large error bars, the apparent capture cross-section can differ considerably from the
416 cross-section directly measured from the filling kinetics ($\sigma_{n\infty}$).

417 Despite the success of DLTS in the identification of deep traps in semiconduc-
418 tors, this technique faces severe difficulties in discriminating traps with close emis-
419 sion/capture kinetics. This is the case of impurities under the effect of slightly different
420 fields, for instance, impurities in alloys with different neighbors (strain fields), or more
421 importantly in the present context, for defects located at hexagonal or pseudo-cubic
422 sites of the 4*H*-SiC lattice. To overcome this problem, the most successful method has
423 been Laplace-DLTS [47]. This method is based on the acquisition and averaging of the
424 emission transient at a constant temperature, followed by an inverse Laplace transform
425 of the signal. This allows for the extraction of individual contributions within the ac-
426 quired data, and leads to an energy resolution of one order of magnitude higher than
427 conventional DLTS.

428 *4.1. As-grown defects in epitaxial 4H-SiC*

429 The main life-time limiting defect (also referred to as "life-time killer") in as-grown
430 4*H*-SiC material is the carbon vacancy. The defect is detected by DLTS as a conspic-
431 uous peak around room temperature, and it was earlier designated by EH2 or more
432 commonly by $Z_{1/2}$ [88, 89]. A typical $Z_{1/2}$ spectrum consists of an asymmetric peak as
433 shown in Figure 7 (see for instance Ref. 86). It is the dominant trap in as-grown epi-
434 taxial 4*H*-SiC, showing up with concentrations in the range 10^{12}-10^{13} cm^{-3}. In order
435 to account for the peak asymmetry, the figure also includes a simulated DLTS signal
436 (solid line), which was fitted to the data in order to reproduce a superposition of two
437 close peaks. The resulting activation energies for electron emission are $\Delta E_1 = 0.59$ eV
438 and $\Delta E_2 = 0.67$ eV, respectively (see legend in the figure). The $Z_{1/2}$ defect is rather
439 stable, sustaining thermal treatments of up to 1400 °C [90].

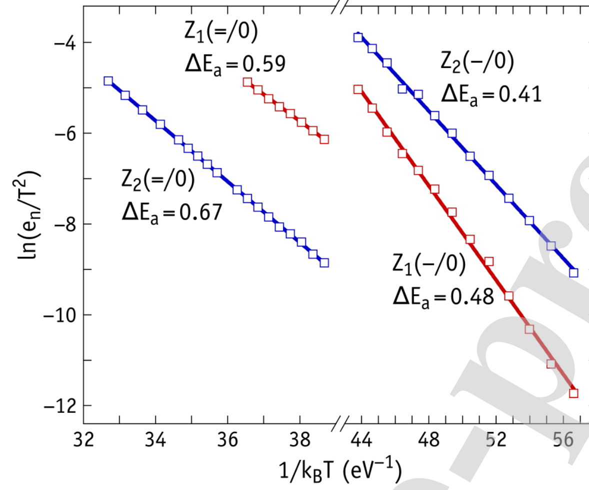

Figure 8: Arrhenius plots of electron emission rates for $Z_1(=/0)$, $Z_2(=/0)$, $Z_1(-/0)$ and $Z_2(-/0)$ transitions in 4*H*-SiC obtained by Laplace-DLTS measurements. Activation energies for electron emission (ΔE_a) are also shown for each peak. Reproduced from Ref. 86, with the permission of AIP Publishing.

440

441 Hemmingsson *et al.* [91] assigned $Z_{1/2}$ to the superposition of two very close 442 DLTS signals, each arising from a sequential emission of two electrons, thus showing 443 negative-*U* ordering of levels. More recently, their connection with electron paramag-444 netic resonance data, allowed the unambiguous identification of $Z_{1/2}$ with the carbon 445 vacancy [92].

446 Recently, Capan and co-workers were able to clarify the carrier emission and cap-447 ture dynamics of $Z_{1/2}$ by applying conventional and Laplace-DLTS in combination with 448 first-principles modeling [65, 86]. The broad $Z_{1/2}$ peak was after all found to comprise 449 a total of four distinct emission processes [65, 86], consisting of single electron emis-450 sions $(-/0)$ and double electron emissions $(=/0)$, each involving the carbon vacancy 451 located on the k and h sites of the 4*H*-SiC lattice. These are often labeled $V_C(k)$ and 452 $V_C(h)$ defects, respectively. The resulting Arrhenius plots from the high-resolution 453 Laplace-DLTS method are shown in Figure 8.

454

455 Based on a comparison between the relative depth of the traps with the respective

Journal Pre-proof

Journal Pre-proof

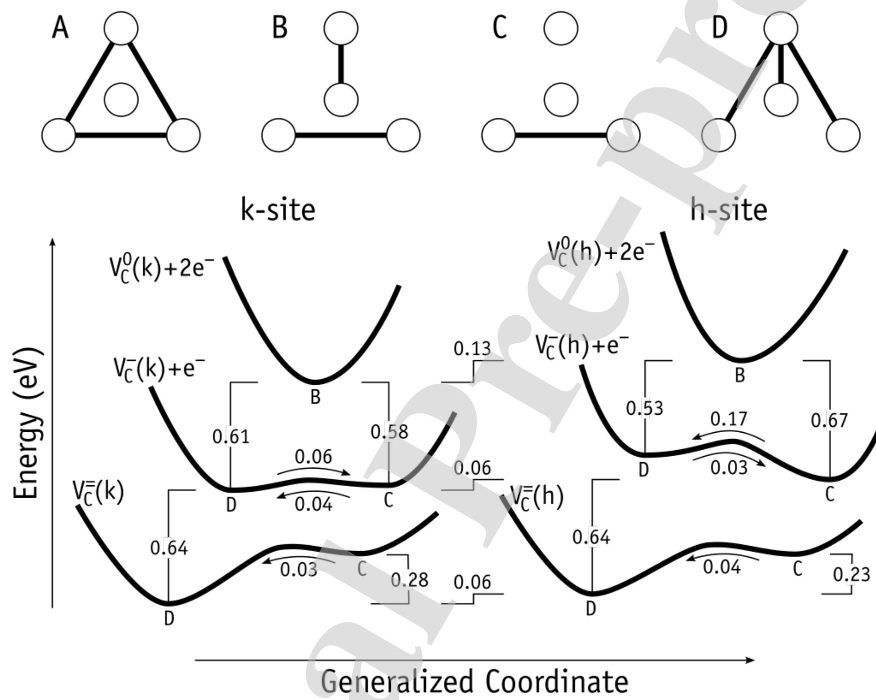

Figure 9: (Top) Possible structures of the carbon vacancy in 4*H*-SiC for several charge states. The [0001] axis is perpendicular to the plane of the figure. Si atoms are shown as white circles. The missing C-atom lies below the central Si atom. Thick lines indicate the formation of reconstructed bonds between Si second neighbors. (Bottom) configuration coordinate diagram for neutral, negative, and double negative V_C defects in n-type 4*H*-SiC. Transformation barriers are indicated next to the arrows. All energies are in eV. Reproduced from Ref. 86, with the permission of AIP Publishing.

Journal Pre-proof

Journal Pre-proof

456 calculations, and a comparison between the relative amplitudes of the emission signals
457 with the calculated relative stability of $V_C(k)$ and $V_C(h)$, it was possible to assign $V_C(k)$
458 and $V_C(h)$ to Z_2 and Z_1 signals, respectively. Both Z_1 and Z_2 showed a negative-U
459 ordering of the acceptor levels. Z_2 had the larger correlation energy ($U = -0.23$ eV)
460 with levels at $E(-/0) = E_c - 0.41$ eV and $E(=/-) = E_c - 0.64$ eV, while Z_1 had levels
461 separated by only $U = -0.11$ eV, and they were found at $E(-/0) = E_c - 0.48$ eV and
462 $E(=/-) = E_c - 0.59$ eV [86]. The capture kinetics was also investigated for $Z_{1/2}$. Only
463 $Z_2(=/-)$ had a measurable capture barrier (0.03 eV), making the activation energy for
464 the doubly charged Z_2 emission 0.67 eV (c.f. Figure 8). The capture mechanisms were
465 found to involve the transformation between different structures of the vacancy. This
466 conclusion is in line with the negative-U character of the defect, which must involve
467 strong relaxations upon changing the charge state [93].

468 For the sake of example, let us look at Figure 9, in particular at the configuration
469 coordinate diagram of vacancies located at the pseudo-cubic sites, $V_C(k)$. Before the
470 filling pulse is applied, the sample diode is reverse biased and all vacancies are in
471 the neutral charge state. Upon injection of majority carriers, electrons are captured
472 by $V_C^0(k, B)$ and their structure quickly transforms to$V_C^-(k, D)$. The binding energy of
473 the electron to the defect (trap depth) was measured as 0.41 eV [86] and calculated
474 as 0.61 eV [76]. Due to the negative-U ordering of levels, $V_C^-(k, D)$ is more *eager*
475 for electrons than $V_C^0(k, B)$ and if free electrons are still available in the conduction
476 band, negatively charged defects will actually capture a second electron at a rate faster
477 than that of the first capture. The binding energy of the second electron captured was
478 measured as 0.64 eV (calculated as 0.64 eV [76]). Analogous results were found for
479 the vacancy at the hexagonal site.

480 The presence of carbon vacancies in SiC seems unavoidable. The reason stems
481 from its rather low formation energy. This quantity was estimated by first-principles
482 within hybrid density functional theory [76, 94] as 5.0 eV and 4.4 eV under C-rich
483 and Si-rich growth conditions, respectively. The C-rich results agree very well with
484 a formation enthalpy of 4.8-5.0 eV as measured from samples grown under the same
485 conditions [41, 95]. The above figures are also consistent with an equilibrium concen-
486 tration in the range 10^{12}-10^{13} cm^{-3} of V_C defects at 1200 °C. This is the temperature

Journal Pre-proof

487 below which the vacancy becomes immobile during sample cool down [60] and the
488 concentration range corresponds to what is usually detected by DLTS [65, 86].

489 *4.2. Defects in 4H-SiC produced by neutron irradiation*

490 Characterization of defects created by ionizing radiation in epitaxial 4*H*-SiC layers
491 is crucial for future improvement of radiation hardness and extending the lifetime of
492 4*H*-SiC detectors by material engineering. The change in performance of SiC-based
493 detectors subject to irradiation by thermal and fast neutrons has been investigated in
494 the past [23, 29, 34, 96].

495 The response stability of SiC SBD detectors with respect to the thermal neutron flu-
496 ence was previously reported by the Westinghouse group [14, 97]. They demonstrated
497 that the devices showed a linear response (measured as count rates) with respect to
498 exposure to fluence rates in the range 10^1-10^8 $cm^{-2}s^{-1}$. The relative precision of the
499 detector (with respect to NIST-calibrated neutron fields) was about 0.6% across six or-
500 ders of magnitude. In addition, the thermal-neutron response of a detector previously
501 irradiated with a fast-neutron ($E > 1$ MeV) fluence of 1.3×10^{16} cm^{-2} was indistin-
502 guishable from that of an non-irradiated SiC detector.

503 More recently, Liu and co-workers [98] investigated the radiation tolerance of SiC
504 against Si neutron detectors. The devices showed significant differences in terms of
505 performance degradation. While Si detectors significantly degraded at a neutron flu-
506 ence of 1.6×10^{13} cm^{-2} — this was quantified by a marked increase in dark current
507 (over four orders of magnitude) and a severe (95%) reduction in the alpha-particle peak
508 centroid, almost no degradation was found for the SiC-based detector, even for neutron
509 fluences up to 3.8×10^{13} cm^{-2}.

510 Performance loss of radiation detectors is usually attributed to a degradation of the
511 life-time of carriers, which become trapped and recombine at defects. Unfortunately,
512 the number of attempts to correlate the degradation of detection with the introduction
513 of defects by neutron impact/reactions is rather limited [34, 66, 99]. This contrasts
514 with the large amount of DLTS studies carried out on ion-implanted, electron- and
515 proton-irradiated SiC samples and devices. For instance, highly energetic alpha par-
516 ticles (which are a common product from neutron reactions) are known to introduce

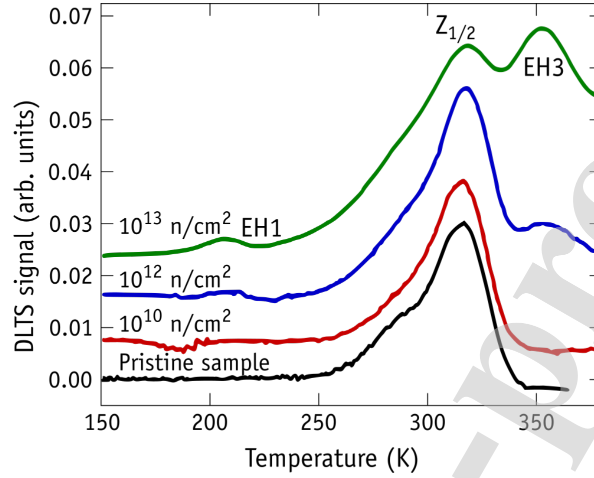

Figure 10: DLTS spectra of as-grown (pristine) and neutron-irradiated 4*H*-SiC SBDs with fluences of 10^{10} n/cm^2, 10^{12} n/cm^2, and 10^{13} n/cm^2 (shown as red, blue and green lines, respectively). The emission rate was 50 s^{-1}. Voltage settings were reverse bias $V_r = -10$ V, pulse bias $V_p = -0.1$ V and pulse width $t_p = 10$ ms. Adapted from Ref. 66.

several defects in 4*H*-SiC [100].

Besides increasing the intensity of $Z_{1/2}$ and EH6/7 signals (which are related to carbon vacancies already present in as-grown material), irradiation of n-type 4*H*-SiC with electrons or protons leads to the appearance of a pair of DLTS peaks labeled EH1/EH3 [89, 101–103] (but also referred to as S1/S2 [90, 104] or S2/S4 [105, 106]) with activation energies of electron emission to the conduction band measured as 0.4 and 0.7 eV, respectively [100, 107]. In recent experimental and theoretical investigations, EH1 and EH3 (or S1 and S2) DLTS levels were identified as Si vacancies in difference sites of the 4H-SiC crystal [108]. Interestingly, while they induce strong compensation effects, they have little impact on the charge collection efficiency of devices [105].

In our experiments, Schottky diodes were irradiated either upon bare exposure or inside Cd thermal neutron filters with a wall thickness of 1 mm. The neutron source provided fluences in the range from (10^8-10^{15} n/cm^2). Figure 10 shows DLTS spectra measured on as-grown 4*H*-SiC (black line) and in neutron-irradiated material with

Journal Pre-proof

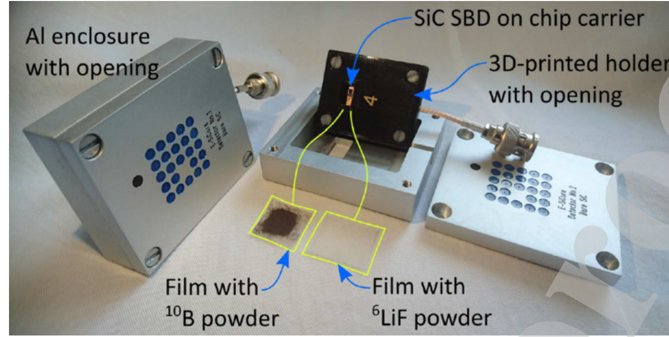

Figure 11: Prototype detectors. Left: assembled detector prototype in aluminum enclosure. Right: prototype detector components: SiC SBD mounted onto chip carrier with contacts, installed in 3D printed holder with opening, converter films (with ^{10}B and ^{6}LiF powder), open aluminum enclosure with opening [63].

532 three different fluences (10^{10} n/cm^2, 10^{12} n/cm^2 and 10^{13} n/cm^2). In as-grown material
533 only the $Z_{1/2}$ peak is observed at around 300 K. Epithermal and fast neutron irradia-
534 tion with fluence up to 10^{11} n/cm^2 did not introduce any traps detectable in the DLTS
535 spectra within the range of temperatures considered. Peaks labeled EH1 and EH3 ap-
536 pear for higher neutron fluences and can be clearly observed for neutron fluences of
537 10^{12} n/cm^2 and 10^{13} n/cm^2.

538 Laplace-DLTS measurements of EH1 and EH3 did not reveal any peak splitting
539 (due to sub-lattice location effects) although the peaks were broad. This suggests that
540 should EH1 and EH3 arise from point defects, Laplace-DLTS was not able to resolve
541 those located on pseudo-cubic and hexagonal sites. Despite that, activation energies
542 for electron emission and apparent capture cross sections were determined as ΔE_{a} =
543 0.397 eV and $\sigma_{\mathrm{a}} = 2 \times 10^{-15}$ cm^{-2} for EH1, and ΔE_{a} = 0.70 eV and $\sigma_{\mathrm{a}} = 1 \times$
544 10^{-15} cm^{-2} for EH3 [66]. These figures are comparable to those obtained by Alfieri
545 and Mihaila [109], although the capture cross section of EH3 differs by about one order
546 of magnitude. Besides the inherent large error bars in the measurement of these pre-
547 exponential quantities, the EH3 signal overlaps the conspicuous $Z_{1/2}$ peak, making the
548 measurement of σ_{a} even more difficult.

549

550 In terms of the impact of neutron radiation on the performance of the SBD de-

Journal Pre-proof

551 tectors, temperature dependent *I-V* measurements of the SBDs revealed that the fast
552 neutron irradiation did not affect the transport properties of the detectors for neu-
553 tron fluences lower that 10^{12} n/cm^2. This confirms the excellent radiation hardness
554 of SiC materials. An increase in the series resistance and decrease of the capacitance
555 of neutron irradiated samples was only observed for neutron fluences of 10^{12} n/cm^2
556 and above, followed by even more pronounced changes in the sample irradiated with a
557 fluence of 10^{13} n/cm^2. The above fluence threshold correlates with the evolution of the
558 DLTS spectrum shown in Figure 10. The increase in series resistance could therefore
559 be related to the capture of free carriers due to the introduction of deep traps like $Z_{1/2}$
560 and EH1/EH3. We note that the impact of deep traps on IV and CV response depends
561 on several factors like their depth within the band gap, cross sections for capture of car-
562 riers, their concentration and location within the structure. $Z_{1/2}$ is omnipresent (even
563 in as-grown conditions) and increases in irradiated material, where its concentration is
564 always higher than EH1 and EH3. This is probably because its production involves a
565 lower displacement energy threshold. Although it is not clear why $Z_{1/2}$ is more harm-
566 ful, a possible reason is that while EH1/EH3 are traps relatively close to the conduction
567 band and they have acceptor character [108], the carbon vacancy ($Z_{1/2}$) also has donor
568 levels close to mid-gap and they are expected to have considerable capture cross section
569 for holes (minority carriers), thus leading to efficient recombination.

570 **5. Testing of a neutron detector prototype**

571 This section presents the experimental activities performed at the JSI TRIGA reac-
572 tor (Ljubljana, Slovenia) [110–113], where a set of SiC-based neutron detectors were
573 tested, some of them being equipped with a thermal neutron converter layer enriched
574 with ^{10}B and ^{6}LiF isotopes. The aspects regarding (1) defect production under neutron
575 irradiation (Figure 10) and (2) detection sensitivity reported in this section were carried
576 out in different experiments. In the study of neutron induced defects, *I-V* characteristics
577 of the irradiated diodes were measured before and after irradiation. The measured re-
578 sults show excellent rectifying properties before and after irradiation, which indicates
579 that the detection properties are not expected to change appreciably after irradiation

Journal Pre-proof

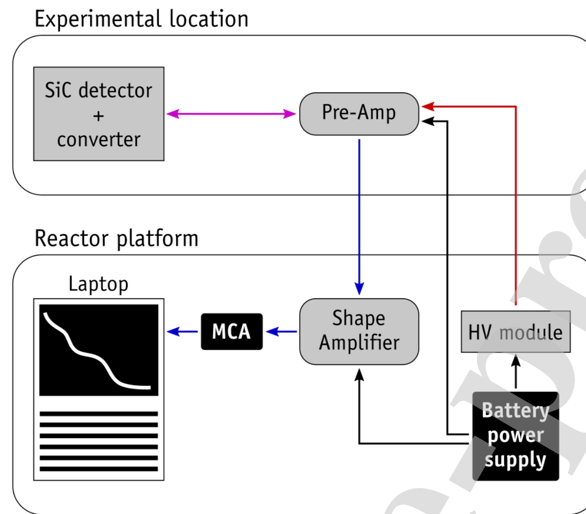

Figure 12: Schematic diagram of the particle event acquisition system. Adapted from Ref. 62.

580 [66, 114]. Further details regarding the sensitivity testing experiments are available
581 elsewhere [62, 63].

582 The detectors were 4*H*-SiC SBDs fabricated at the National Institute for Quantum
583 and Radiological Science and Technology (QST, Japan). The SiC epitaxial layer was
584 n-type doped, with thickness and nitrogen concentration in the range 25-170 μm and
585 (4.7-9.1) $\times$ 10^{14} cm^{-3}, respectively. Schottky and Ohmic contacts were fabricated by
586 deposition and sintering of nickel front and back contacts, respectively. The SBDs had
587 lateral dimension of 1 mm $\times$ 1 mm, and they were surface-mounted onto chip carriers
588 with wire bonded electrical contacts. Figure 11 shows the components of the detector
589 employed in the tests reported below [115]. The structures were electrically isolated
590 by enclosure within 3D-printed plastic holders encapsulated by aluminum cases. Both
591 the cases and holders had a window through which radiation could hit the SBDs.

592

593 The detectors were equipped with a thermal neutron converting layers consisting of
594 ^{10}B and ^{6}LiF-enriched powders. These substances contain isotopes which are among
595 those with largest thermal neutron cross sections for (n, α) and (n, t) reactions (around
596 3843 barn and 938 barn respectively, at an incident neutron energy of 0.0253 eV [116]).

Journal Pre-proof

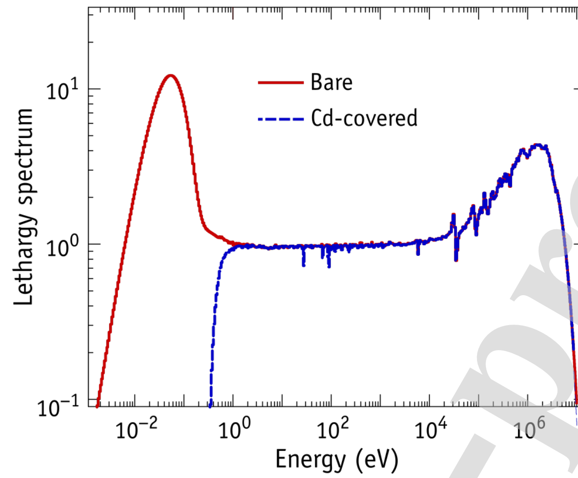

Figure 13: Neutron spectra of the Pneumatic Tube irradiation channel, located in the F24 core position of the JSI TRIGA reactor. Solid red line: bare spectrum. Dashed blue line: spectrum under Cd coverage [62].

597 The converting materials were applied onto a plastic film and mounted above the open-
598 ings of the 3D-printed SBD holders. The distance between the thermal neutron convert-
599 ing layers and the SBD top surface was approximately 2 mm. In the work presented
600 in this section the thickness of the converting layers was not well controlled. This
601 prompted us to study in detail the optimization of the converting layer thickness, and
602 from there, to maximize the detection efficiency. This will be carrier out on the basis
603 of calculations with the SRIM (stopping range in matter) and MCNP (Monte Carlo
604 N-Particle transport) codes.

605 Figure 12 displays a schematic diagram of the electronic data acquisition system
606 that was assembled for the tests. The electronic system for particle event processing and
607 recording consisted of a preamplifier followed by shaping amplifier and a multichannel
608 analyzer (MCA), operated by a laptop computer. In order to avoid noise from the mains
609 power, the system was powered by a standalone battery voltage source. The latter also
610 provided power to a separate high voltage module (HV module in Figure 12), which
611 was used to apply a reverse bias to the SBDs.

612

613 In order to keep a low capacitance input (10 pF) to the pre-amplifier stage, we used a

Journal Pre-proof

Journal Pre-proof

614 CREMAT CR110-R2 pre-amplifier chip and tested the detection energy resolution with
615 the shaping PCB module equipped with a CR-200-R2 chip with shaping times of 0.5 μs
616 and 1.0 μs. The total gain for event signal amplification was kept constant. Pole/Zero
617 (P/Z) was adjusted for different shaping constants. Recorded events were sorted by
618 the MCA in 2k-channel energy spectra. The performance of the detection system was
619 observed for shaping times of 0.5 μs and 1.0 μs and reverse bias voltages of 50 V and
620 100 V. The combination of a reverse bias voltage of 50 V and a shaping time of 1 μs
621 resulted in best spectroscopic performance. The amplitude of the reverse bias pulse
622 (for a specific epi-layer thickness) was not optimized. That should be systematically
623 tested in the future.

624 The neutron spectrum (Figure 13) was calculated by using a Monte Carlo neutron
625 transport code MCNP [117] in conjunction with the ENDF/B-VIII.0 nuclear data li-
626 brary [118]. A verified and validated computational model of the JSI TRIGA reactor
627 was employed, based on the JSI TRIGA criticality benchmark model [119], featured
628 in the International Handbook of Evaluated Critical Safety Benchmark Experiments
629 [120].

630 Neutron irradiations were performed in the Dry Chamber of the JSI TRIGA reactor.
631 This is located in the concrete body of the reactor, being connected the core through
632 a graphite thermalizing column [121]. It has been used for radiation hardness testing
633 of detectors, electronic components and systems [122, 123]. In order to determine the
634 neutron flux, activation dosimetry measurements were carried out using foils of certi-
635 fied reference material Al-0.1 wt.% Au, obtained from the IRMM (now Joint Research
636 Center - JRC, Geel, Belgium). These were irradiated to measure the ^{197}Au(n, γ)^{198}Au
637 reaction rate, the cross-section for this nuclear reaction being a standard. The neutron
638 flux is linearly proportional to the reactor power, which was varied between 10 kW
639 and 250 kW (maximum steady state power). At full power the total neutron flux was
640 1.6×10^7 n/cm^{2}s. Further details may be found in Ref. 62.

641

642 Figure 14 shows the measured spectra of SiC detectors placed in the Dry Chamber
643 of the reactor at different power levels (along with respective flux values). Spectra for
644 detectors with either a ^{10}B or ^{6}LiF converter layers are reported. In all the recorded

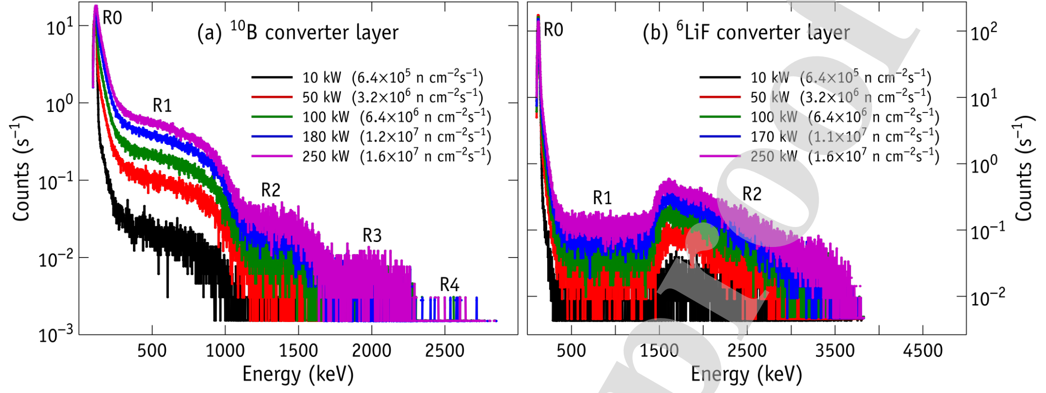

Figure 14: Measured count spectra of SiC detectors placed in the Dry Chamber of the reactor at different power levels (next to respective flux values within parentheses). The thickness of the SBD epi-layer was 69 μm. (a) Spectrum of a detector covered with a ^{10}B converter layer and (b) Spectrum of a detector covered with a ^{6}LiF converter layer [62].

645 spectra a significant number of counts at higher energy channels was observed. Dis-
646 tinctive structures were also obtained, depending on the converter layer employed.

647 The relevant neutron reactions leading to the production of charged particles are
648 either ^{10}B(n, α)^{7}Li or ^{6}Li(n, α)t [63]. The first one has two possibilities with respective
649 branching ratios (BR),

$$^{10}\mathrm{B} + \mathrm{n} \rightarrow \alpha\,(1776\,\mathrm{keV}) + {}^{7}\mathrm{Li}\,(1013\,\mathrm{keV});\ \mathrm{BR} = 6.3\%;\ Q = 2789.5\,\mathrm{keV}$$

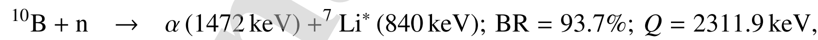

$$^{10}\mathrm{B} + \mathrm{n} \rightarrow \alpha\,(1472\,\mathrm{keV}) + {}^{7}\mathrm{Li}^{*}\,(840\,\mathrm{keV});\ \mathrm{BR} = 93.7\%;\ Q = 2311.9\,\mathrm{keV},$$

650 where ^{7}Li* is an excited state of ^{7}Li and Q the reaction Q-value. Conversely, ^{6}Li(n, α)t
651 follows as,

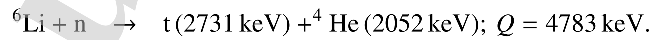

$$^{6}\mathrm{Li} + \mathrm{n} \rightarrow \mathrm{t}\,(2731\,\mathrm{keV}) + {}^{4}\mathrm{He}\,(2052\,\mathrm{keV});\ Q = 4783\,\mathrm{keV}.$$

652 The spectra of Figure 14 display distinctive structures, which can be assigned to
653 the recording of secondary charged particles originating from ^{10}B(n, α) and ^{6}Li(n, t)
654 reactions. The main features (regions) in the spectra are denoted as “R0-4” and “R0-
655 2” in Figures 14(a) and 14(b), respectively. The sharp peak R0 that is present in both

Journal Pre-proof

Journal Pre-proof

656 spectra at low energy channels is attributed to electronic noise. Inspection of the kinetic
657 energy of the reaction products against the spectra allowed a tentative assignment of
658 the spectral features.

659 For the ^{10}B-covered detectors [Figure 14(a)], R1 was connected to hits by ^{7}Li (E =
660 1013 keV) and ^{7}Li* (E = 840 keV) ions, R2 was assigned to alpha particles (E =
661 1776 keV or E = 1472 keV), R3 was assigned to a combined detection of alphas and
662 ^{7}Li* from the dominant reaction, while R4 was attributed to the analogous combined
663 detection of alphas and ^{7}Li from the less probable reaction branch.

664 The above assignments are tentative, as there is observable overlap between re-
665 gions and no clear peaks appearing. This is probably due to (i) a partial energy loss
666 of the secondary particles in the converter / air gap / front contact, and (ii) a lim-
667 ited detection resolution. The assignments are made on the basis of the drops in the
668 pulse height spectra observed on the high energy side of each region. R1 drops off at
669 slightly above 1000 keV, corresponding to the maximum ^{7}Li energy (1013 keV), R2
670 drops off at approximately 1700 keV, corresponding to the maximum energy thresh-
671 old of alpha particles (1776 keV). R3 in particular drops off very sharply at approxi-
672 mately 2300 keV, corresponding very well to the maximum detectable particle energy
673 from the dominant ^{10}B(n,α) reaction channel (1472 keV + 840 keV = 2312 keV). R4
674 has the least number of counts, and seems to end at above 2700 keV, correspond-
675 ing to the maximal detectable particle energy from the less probable reaction channel
676 (1776 keV + 1013 keV = 2789 keV).

677 For the spectra obtained using the ^{6}LiF converter layer [Figure 14(b)], the fea-
678 tures were not so well resolved and the interpretation was more difficult and tenta-
679 tive. Accordingly, the R1 plateau was connected to partial energy deposition events,
680 while R2 was attributed to a combination of partial energy deposition from tritons
681 (E = 2731 keV) and alpha particles (E = 2052 keV).

682 Among the most important specifications of a neutron detector are its sensitivity
683 and response linearity. In order to minimize electronic noise of a real-life detection
684 system, the signal recorded should be derived from the total counts above a certain
685 channel number (energy threshold). Radulovi and co-workers [62] set this threshold at
686 around 600 keV, which is definitely above the R0 peak of Figures 14(a) and 14(b), and

Journal Pre-proof

Journal Pre-proof

687 obtained total detected count rates as a function of reactor power and corresponding
688 neutron flux as depicted in Figure 15. The figure shows excellent response linearity,
689 irrespectively of the converter layer employed or the thickness of the epitaxial 4H-SiC
690 front layer. The sensitivity of the detector per unit of neutron flux is given by the
691 slope in the graphs. On average, these were found to be over 10^{-5} (counts/s)/(n/cm^{2}s)
692 [62]. In Figure 15, the data labeled with "170 μm, ^{10}B (1)" and "170 μm / ^{10}B (2)"
693 refer to separate measurements with the same 170 μm thick detector, but different ^{10}B
694 converters. The difference in the results suggests a dependence of the flux of ionizing
695 particles hitting the SiC diode with respect to the converter layer thickness.

696 It becomes apparent from Figure 15 that for the same ^{10}B conversion layer, the
697 thinner epi-SiC layer leads to higher sensitivity. We note that the sensitivity for ther-
698 mal neutrons is mostly determined by the properties of the conversion layer. Hence,
699 given (i) the limited amount of samples and (ii) the lack of detail regarding the charac-
700 terization of the conversion layers, we cannot draw a conclusion regarding thickness-
701 sensitivity trends. In the present work, the detection sensitivity is primarily dependent
702 on the use of either ^{6}LiF or ^{10}B layers. The decay products of the ^{6}Li include highly
703 energetic tritons, whose penetration depth and efficiency in terms of electron-hole cre-
704 ation could be more favorable than that of the alpha particles from ^{10}B.

705 Improvements to the sensitivity of detectors based on SiC-SBD could in principle
706 be achieved by increasing the cross-section area of the active region, *i.e.* by enlarging
707 the area of the semiconductor layers. This route is hindered by two factors, namely
708 (i) a decrease in the fabrication yield and (ii) an increase of the SBD capacitance
709 which at some point becomes detrimental and lowers the sensitivity. Future large-area
710 semiconductor-based detectors are therefore likely to be pixelized. However, this has
711 the disadvantage of increasing the complexity of fabrication and maintenance, includ-
712 ing a much more complex read-out electronics and data processing.

713 The neutron fluxes considered in the measurements of Ref. [62] are at least 6 orders
714 of magnitude larger than the background neutron flux at the Earth surface [124]. This
715 is the critical benchmark which any detector relevant for home-land security will have
716 to comply with, particularly if the aim is to screen for disguised radiological materials.
717 Commercially available $^{10}BF_3$ and ^{3}He detectors show sensitivity values of the order

Journal Pre-proof

718 of 4 (counts/s)/(n/cm^{2}s) and 10-100 (counts/s)/(n/cm^{2}s), respectively. Their size are
719 in range 2.5-5.1 cm (1-2 inches) in diameter and 0.3-1.8 m long. For comparison, a
720 100×1000 pixelized SiC detectors with the above reported sensitivity, would show an
721 overall sensitivity of around 1 (counts/s)/(n/cm^{2}s). We must mind though, that current
722 neutron sensitivity of SiC-based detectors is limited and its application on the field
723 would imply very large detector arrays, which in turn would require a high degree of
724 system complexity and serious technical challenges related to the implementation and
725 operation.

726 6. Conclusions

727 We presented a review about the workings of SiC-based neutron detectors along
728 with several issues related to material properties, device fabrication and testing. The
729 paper summarizes the work carried within the E-SiCure project (*Engineering Silicon*
730 *Carbide for Border and Port Security*), funded by the NATO Science for Peace and
731 Security Programme. The main goal was the development of material and device tech-
732 nologies to support the fabrication of radiation-hard silicon carbide (SiC) based detec-
733 tors of special nuclear materials, envisaging the enhancement of border security and
734 customs screening capability. Achievements include the fabrication of a 4H-SiC based
735 SBD detector equipped with a thermal neutron converter layer, as well as the charac-
736 terization of the main carrier traps affecting the performance before and after exposure
737 of the devices to neutron fields.

738 We started the first section of the paper by justifying the significance of developing
739 a neutron detection technology that could match that based on ^{3}He. The advantages
740 of semiconductor-detectors were enumerated, in particular those of devices based on
741 the 4*H* polytype of silicon carbide (4*H*-SiC), including its radiation hardness and elec-
742 tronic specifications. We described the basic structure of a detector based on a 4*H*-SiC
743 Schottky barrier diode covered with a thermal neutron converter layer. Here we went
744 through the main physical processes taking place, from the impact of a neutron until
745 the collection of charge carriers at the terminals. The importance of understanding and
746 controlling the presence of defects in the semiconductor was highlighted based on their

Journal Pre-proof

747 impact on the carrier life-time and sensitivity of the detector.

748 In Section 2 we revised the main properties of SiC materials, namely its poly-
749 typism and introduced the common crystallographic notations employed. The optical
750 and electronic transport properties of SiC were also described, including the band gap
751 width and its dependence with the polytype. We then proceeded to Section 3, where
752 the material (4*H*-SiC) growth and device fabrication was addressed. We started by de-
753 scribing the different types of growth techniques involving seeding as well as bulk and
754 epitaxial growth. The fabrication of a Schottky barrier diode was described, namely
755 the formation of Schottky and Ohmic contacts.

756 We dedicated considerable effort to the identification, characterization and model-
757 ing of defects in as-grown and neutron irradiated 4*H*-SiC. The defect which is most
758 detrimental to the electronic performance of the devices gives rise to a prominent sig-
759 nal detected by deep level transient spectroscopy. This signal is commonly labeled as
760 $Z_{1/2}$, and arises from a carbon vacancy. A total of four electronic transitions in the
761 gap were resolved experimentally. With the help of theoretical modeling, they were
762 all assigned to carbon vacancies in different lattice sites and charge states. Controlling
763 the concentration of this defect seems to be critical to improve the performance of the
764 diodes.

765

766 The development and testing of a SiC SBD neutron detector prototype and acqui-
767 sition system was described in Section 5. It was shown that detectors based on SiC
768 SBDs and equipped with thermal neutron converter films (enriched with ^{10}B and ^{6}LiF
769 isotopes) clearly show a neutron response with excellent linearity. Arrays of such de-
770 tectors are anticipated to offer sensitivities close to those currently available in the
771 market.

772 The above results stand as a motivation for future improvements of SiC-based neu-
773 tron detectors. In fact there is ample room for improvement and several key factors
774 influencing the sensitivity of the detectors are worthy of investigating. These include
775 decreasing the concentration of deep carrier traps during growth, optimizing the charge
776 collection active volume, avoiding an air layer between the converter material and the
777 SBD top surface by enclosing the device in a vacuum chamber, optimizing the thick-

Journal Pre-proof

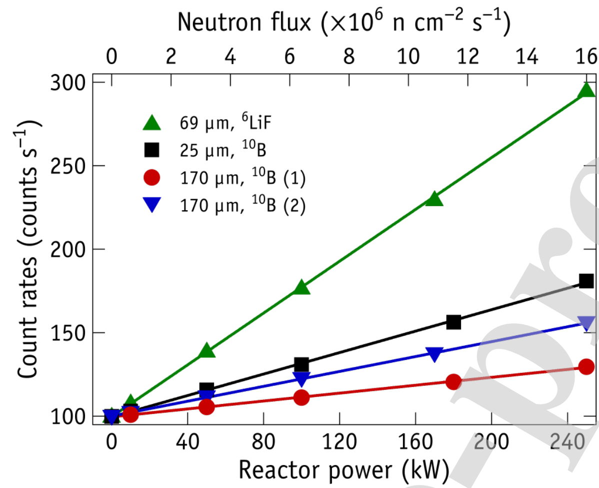

Figure 15: Total detected count rates above channel no. 500 (around 600 keV), as a function of reactor power and respective neutron flux. Four different diodes with varying thickness of the 4*H*-SiC layer and type of converter materials (see legend) were considered. Adapted from Ref. 62.

778 ness of the converter layer, among others.

779 Acknowledgements

780 The present work was financially supported by the NATO Science for Peace and 781 Security Programme, under project no. 985215 - *Engineering Silicon Carbide for Bor-* 782 *der and Port Security* – E-SiCure. The JSI project team acknowledge the financial 783 support from the Slovenian Research Agency (research core funding No. (P2-0073). 784 The RBI project team would like to acknowledge financial support from the European 785 Regional Development Fund for the Center of Excellence for Advanced Materials and 786 Sensing Devices (Grant No. KK.01.1.1.01.0001), European Unions Horizon 2020 Re- 787 search and Innovation Programme, grant number 669014, European Union through 788 the European Regional Development Fund – The Competitiveness and Cohesion Op- 789 erational Programme, grant number KK.01.1.06. JC thanks the support of the i3N 790 project, Refs. UIDB/50025/2020 and UIDP/50025/2020, financed by the Fundação 791 para a Ciência e a Tecnologia in Portugal. The ANSTO team wishes to acknowledge 792 the National Collaborative Research Infrastructure Strategy funding provided by the

Journal Pre-proof

793 Australian Government for this research.

794 **References**

795 [1] S. Fetter, V. A. Frolov, M. Miller, R. Mozley, O. F. Prilutsky, S. N. Rodionov,
796 R. Z. Sagdeev, Detecting nuclear warheads, Science & Global Security 1 (3-4)
797 (1990) 225–253. doi:10.1080/08929889008426333.

798 [2] S.-H. Park, J.-S. Park, H.-Seo, S. K. Lee, H.-S. Shin, H. D. Kim, Development
799 of SiC detector for the harsh environment applications, in: 2013 IEEE Nuclear
800 Science Symposium and Medical Imaging Conference (2013 NSS/MIC), IEEE,
801 2013. doi:10.1109/nssmic.2013.6829850.

802 [3] A. Glaser, B. Barak, R. J. Goldston, A zero-knowledge protocol for nuclear war-
803 head verification, Nature 510 (7506) (2014) 497–502. doi:10.1038/nature13457.

804 [4] R. T. Kouzes, J. H. Ely, L. E. Erikson, W. J. Kernan, A. T. Lintereur, E. R. Sicil-
805 iano, D. L. Stephens, D. C. Stromswold, R. M. V. Ginhoven, M. L. Woodring,
806 Neutron detection alternatives to ^{3}He for national security applications, Nu-
807 clear Instruments and Methods in Physics Research Section A: Accelerators,
808 Spectrometers, Detectors and Associated Equipment 623 (3) (2010) 1035–1045.
809 doi:10.1016/j.nima.2010.08.021.

810 [5] A. Wahbi, L. Heng, G. Dercon, Cosmic ray neutron sensing: estimation of
811 agricultural crop biomass water equivalent, Springer, Cham, Switzerland, 2018.
812 doi:10.1007/978-3-319-69539-6.

813 [6] T. Kimoto, Material science and device physics in SiC technology for high-
814 voltage power devices, Japanese Journal of Applied Physics 54 (4) (2015)
815 040103. doi:10.7567/jjap.54.040103.

816 [7] X. She, A. Q. Huang, O. Lucia, B. Ozpineci, Review of silicon carbide power de-
817 vices and their applications, IEEE Transactions on Industrial Electronics 64 (10)
818 (2017) 8193–8205. doi:10.1109/tie.2017.2652401.

Journal Pre-proof

Journal Pre-proof

819 [8] J. Wang, V. Veliadis, J. Zhang, Y. Alsmadi, P. R. Wilson, M. J. Scott,
820 IEEE ITRW working group position paper-system integration and applica-
821 tion: silicon carbide: a roadmap for silicon carbide adoption in power con-
822 version applications, IEEE Power Electronics Magazine 5 (2) (2018) 40–44.
823 doi:10.1109/mpel.2018.2822863.

824 [9] W. J. Choyke, H. Matsunami, G. Pensl (Eds.), Silicon carbide: recent
825 major advances, Advanced texts in physics, Springer-Verlag, Berlin, 2004.
826 doi:10.1007/978-3-642-18870-1.

827 [10] T. Kimoto, J. A. Cooper, Fundamentals of silicon carbide technology: growth,
828 characterization, devices, and applications, John Wiley & Sons Singapore Pte.
829 Ltd, Singapore, 2014. doi:10.1002/9781118313534.

830 [11] F. Nava, P. Vanni, M. Bruzzi, S. Lagomarsino, S. Sciortino, G. Wagner,
831 C. Lanzieri, Minimum ionizing and alpha particles detectors based on epitax-
832 ial semiconductor silicon carbide, IEEE Transactions on Nuclear Science 51 (1)
833 (2004) 238–244. doi:10.1109/tns.2004.825095.

834 [12] F. H. Ruddy, J. G. Seidel, H. Chen, A. R. Dulloo, S.-H. Ryu, High-resolution
835 alpha-particle spectrometry using silicon carbide semiconductor detectors, in:
836 IEEE Nuclear Science Symposium Conference Record, IEEE, 2005, p. 1232.
837 doi:10.1109/nssmic.2005.1596541.

838 [13] G. Lioliou, H. K. Chan, T. Gohil, K. V. Vassilevski, N. G. Wright, A. B.
839 Horsfall, A. M. Barnett, 4H-SiC Schottky diode arrays for X-ray detection,
840 Nuclear Instruments and Methods in Physics Research Section A: Accelera-
841 tors, Spectrometers, Detectors and Associated Equipment 840 (2016) 145–152.
842 doi:10.1016/j.nima.2016.10.002.

843 [14] A. R. Dulloo, F. H. Ruddy, J. G. Seidel, J. M. Adams, J. S. Nico, D. M. Gilliam,
844 The thermal neutron response of miniature silicon carbide semiconductor detec-
845 tors, Nuclear Instruments and Methods in Physics Research Section A: Accel-
846 erators, Spectrometers, Detectors and Associated Equipment 498 (1-3) (2003)
847 415–423. doi:10.1016/s0168-9002(02)01987-3.

Journal Pre-proof

848 [15] F. Franceschini, F. H. Ruddy, Silicon carbide neutron detectors, in: R. Ger-
849 hardt (Ed.), Properties and applications of silicon carbide, InTech, Rijeka, 2011,
850 Ch. 13. doi:10.5772/615.

851 [16] D. Szalkai, R. Ferone, F. Issa, A. Klix, M. Lazar, A. Lyoussi, L. Ottaviani,
852 P. Tutto, V. Vervisch, Fast neutron detection with 4H-SiC based diode detector
853 up to 500 °C ambient temperature, IEEE Transactions on Nuclear Science 63 (3)
854 (2016) 1491–1498. doi:10.1109/tns.2016.2522921.

855 [17] O. Obraztsova, L. Ottaviani, A. Klix, T. Doring, O. Palais, A. Lyoussi, Com-
856 paring the response of a SiC and a sCVD diamond detectors to 14-MeV neu-
857 tron radiation, IEEE Transactions on Nuclear Science 65 (9) (2018) 2380–2384.
858 doi:10.1109/tns.2018.2848469.

859 [18] L.-Y. Liu, L. Wang, P. Jin, J.-L. Liu, X.-P. Zhang, L. Chen, J.-F. Zhang, X.-P.
860 Ouyang, A. Liu, R.-H. Huang, S. Bai, The fabrication and characterization of
861 Ni/4H-SiC Schottky diode radiation detectors with a sensitive area of up to 4
862 cm^2, Sensors 17 (10) (2017) 2334. doi:10.3390/s17102334.

863 [19] M. Marinelli, E. Milani, G. Prestopino, A. Tucciarone, C. Verona, G. Verona-
864 Rinati, M. Angelone, D. Lattanzi, M. Pillon, R. Rosa, E. Santoro, Synthetic
865 single crystal diamond as a fission reactor neutron flux monitor, Applied Physics
866 Letters 90 (18) (2007) 183509. doi:10.1063/1.2734921.

867 [20] M. Angelone, D. Lattanzi, M. Pillon, M. Marinelli, E. Milani, A. Tucciarone,
868 G. Verona-Rinati, S. Popovichev, R. M. Montereali, M. A. Vincenti, A. Mu-
869 rari, Development of single crystal diamond neutron detectors and test at JET
870 tokamak, Nuclear Instruments and Methods in Physics Research Section A: Ac-
871 celerators, Spectrometers, Detectors and Associated Equipment 595 (3) (2008)
872 616–622. doi:10.1016/j.nima.2008.07.107.

873 [21] S. Almaviva, M. Marinelli, E. Milani, G. Prestopino, A. Tucciarone, C. Verona,
874 G. Verona-Rinati, M. Angelone, D. Lattanzi, M. Pillon, R. M. Montereali,

875 M. A. Vincenti, Thermal and fast neutron detection in chemical vapor deposi-
876 tion single-crystal diamond detectors, Journal of Applied Physics 103 (5) (2008)
877 054501. doi:10.1063/1.2838208.

878 [22] F. Pompili, B. Esposito, D. Marocco, S. Podda, M. Riva, S. Baccaro, A. Cemmi,
879 I. D. Sarcina, L. Quintieri, D. Bocian, K. Drozdowicz, M. Curylo, J. Dankowski,
880 J. Kotula, W. Maciocha, T. Nowak, J. Swierblewsk, L. Vermeeren, W. Leysen,
881 M. Passeri, Radiation and thermal stress test on diamond detectors for the radial
882 neutron camera of ITER, Nuclear Instruments and Methods in Physics Research
883 Section A: Accelerators, Spectrometers, Detectors and Associated Equipment
884 936 (2019) 62–64. doi:10.1016/j.nima.2018.10.110.

885 [23] M. Hodgson, A. Lohstroh, P. Sellin, D. Thomas, Characterization of silicon car-
886 bide and diamond detectors for neutron applications, Measurement Science and
887 Technology 28 (10) (2017) 105501. doi:10.1088/1361-6501/aa7f8b.

888 [24] O. Obraztsova, L. Ottaviani, B. Geslot, G. de Izarra, O. Palais, A. Lyoussi,
889 W. Vervisch, Comparison between silicon carbide and diamond for thermal
890 neutron detection at room temperature, IEEE Transactions on Nuclear Science
891 67 (5) (2020) 863–871. doi:10.1109/tns.2020.2981059.

892 [25] F. Nava, G. Wagner, C. Lanzieri, P. Vanni, E. Vittone, Investigation of Ni/4H-
893 SiC diodes as radiation detectors with low doped n-type 4H-SiC epilayers, Nu-
894 clear Instruments and Methods in Physics Research Section A: Accelerators,
895 Spectrometers, Detectors and Associated Equipment 510 (3) (2003) 273–280.
896 doi:10.1016/s0168-9002(03)01868-0.

897 [26] R. W. Flammang, J. G. Seidel, F. H. Ruddy, Fast neutron detection with silicon
898 carbide semiconductor radiation detectors, Nuclear Instruments and Methods in
899 Physics Research Section A: Accelerators, Spectrometers, Detectors and Asso-
900 ciated Equipment 579 (1) (2007) 177–179. doi:10.1016/j.nima.2007.04.034.

901 [27] F. Issa, V. Vervisch, L. Ottaviani, D. Szalkai, L. Vermeeren, A. Lyoussi,
902 A. Kuznetsov, M. Lazar, A. Klix, O. Palais, A. Hallen, Radiation silicon carbide

903 detectors based on ion implantation of boron, IEEE Transactions on Nuclear
904 Science 61 (4) (2014) 2105–2111. doi:10.1109/tns.2014.2320943.

905 [28] F. H. Ruddy, A. R. Dulloo, J. G. Seidel, M. K. Das, S.-H. Ryu, A. K. Agar-
906 wal, The fast neutron response of 4H silicon carbide semiconductor radiation
907 detectors, IEEE Transactions on Nuclear Science 53 (3) (2006) 1666–1670.
908 doi:10.1109/tns.2006.875151.

909 [29] M. Hodgson, A. Lohstroh, P. Sellin, D. Thomas, Neutron detection performance
910 of silicon carbide and diamond detectors with incomplete charge collection
911 properties, Nuclear Instruments and Methods in Physics Research Section A:
912 Accelerators, Spectrometers, Detectors and Associated Equipment 847 (2017)
913 1–9. doi:10.1016/j.nima.2016.11.006.

914 [30] S. Tripathi, C. Upadhyay, C. P. Nagaraj, A. Venkatesan, K. Devan, Towards
915 radiation hard converter material for SiC-based fast neutron detectors, Jour-
916 nal of Instrumentation 13 (05) (2018) P05026–P05026. doi:10.1088/1748-
917 0221/13/05/p05026.

918 [31] V. F. Sears, Neutron scattering lengths and cross sections, Neutron News 3 (3)
919 (1992) 26–37. doi:10.1080/10448639208218770.

920 [32] F. Issa, L. Ottaviani, D. Szalkai, L. Vermeeren, V. Vervisch, A. Lyoussi, R. Fer-
921 one, A. Kuznetsov, M. Lazar, A. Klix, O. Palais, 4H-SiC neutron sensors based
922 on ion implanted ^{10}B neutron converter layer, IEEE Transactions on Nuclear
923 Science 63 (3) (2016) 1976–1980. doi:10.1109/tns.2016.2565439.

924 [33] C. Maples, G. W. Goth, J. Cerny, Nuclear reaction *Q*-values, in: Nuclear Data
925 Sheets Section A, ADS, 1966, p. 429.

926 [34] F. Nava, A. Castaldini, A. Cavallini, P. Errani, V. Cindro, Radiation detection
927 properties of 4H-SiC Schottky diodes irradiated up to 10^{16} n/cm^2 by 1 MeV
928 neutrons, IEEE Transactions on Nuclear Science 53 (5) (2006) 2977–2982.
929 doi:10.1109/tns.2006.882777.

Journal Pre-proof

930 [35] K. C. Mandal, S. K. Chaudhuri, K. Nguyen, An overview of application of 4H-
931 SiC n-type epitaxial Schottky barrier detector for high resolution nuclear detec-
932 tion, in: 2013 IEEE Nuclear Science Symposium and Medical Imaging Confer-
933 ence (2013 NSS/MIC), IEEE, 2013. doi:10.1109/nssmic.2013.6829844.

934 [36] A. R. Peaker, V. P. Markevich, J. Coutinho, Tutorial: Junction spectroscopy
935 techniques and deep-level defects in semiconductors, Journal of Applied Physics
936 123 (16) (2018) 161559. doi:10.1063/1.5011327.

937 [37] C. H. Henry, D. V. Lang, Nonradiative capture and recombination by multi-
938 phonon emission in GaAs and GaP, Physical Review B 15 (2) (1977) 989–1016.
939 doi:10.1103/physrevb.15.989.

940 [38] A. M. Strel'chuk, B. Berenguier, E. B. Yakimov, L. Ottaviani, Recombination
941 processes in 4H-SiC pn structures, Materials Science Forum 858 (2016) 345–
942 348. doi:10.4028/www.scientific.net/msf.858.345.

943 [39] T. Hiyoshi, T. Kimoto, Reduction of deep levels and improvement of carrier life-
944 time in n-type 4H-SiC by thermal oxidation, Applied Physics Express 2 (2009)
945 041101. doi:10.1143/apex.2.041101.

946 [40] L. S. Løvlie, B. G. Svensson, Oxidation-enhanced annealing of implantation-
947 induced $Z_{1/2}$ centers in 4H-SiC: reaction kinetics and modeling, Physical Re-
948 view B 86 (7) (2012) 075205. doi:10.1103/physrevb.86.075205.

949 [41] H. M. Ayedh, A. Hallén, B. G. Svensson, Elimination of carbon vacancies in
950 4H-SiC epi-layers by near-surface ion implantation: influence of the ion species,
951 Journal of Applied Physics 118 (17) (2015) 175701. doi:10.1063/1.4934947.

952 [42] H. M. Ayedh, R. Nipoti, A. Hallén, B. G. Svensson, Thermodynamic equili-
953 bration of the carbon vacancy in 4H-SiC: a lifetime limiting defect, Journal of
954 Applied Physics 122 (2) (2017) 025701. doi:10.1063/1.4991815.

955 [43] L. Storasta, H. Tsuchida, Reduction of traps and improvement of carrier lifetime
956 in 4H-SiC epilayers by ion implantation, Applied Physics Letters 90 (6) (2007)
957 062116. doi:10.1063/1.2472530.

Journal Pre-proof

Journal Pre-proof

958 [44] T. Miyazawa, H. Tsuchida, Point defect reduction and carrier lifetime improvement of Si- and C-face 4H-SiC epilayers, Journal of Applied Physics 113 (8) (2013) 083714. doi:10.1063/1.4793504.

961 [45] H. M. Ayedh, R. Nipoti, A. Hallén, B. G. Svensson, Elimination of carbon vacancies in 4H-SiC employing thermodynamic equilibrium conditions at moderate temperatures, Applied Physics Letters 107 (25) (2015) 252102. doi:10.1063/1.4938242.

965 [46] D. V. Lang, Deep-level transient spectroscopy: a new method to characterize traps in semiconductors, Journal of Applied Physics 45 (7) (1974) 3023–3032. doi:10.1063/1.1663719.

968 [47] L. Dobaczewski, A. R. Peaker, K. B. Nielsen, Laplace-transform deep-level spectroscopy: the technique and its applications to the study of point defects in semiconductors, Journal of Applied Physics 96 (9) (2004) 4689–4728. doi:10.1063/1.1794897.

972 [48] A. Mattausch, Ab-initio theory of point defects and defect complexes in SiC, Ph.D. thesis, University of Erlangen-Nürnberg (2005).

974 [49] T. Hornos, Theoretical study of defects in silicon carbide and at the silicon dioxide interface, Ph.D. thesis, Budapest University of Technology and Economics (2008).

977 [50] R. O. Jones, O. Gunnarsson, The density functional formalism, its applications and prospects, Reviews of Modern Physics 61 (3) (1989) 689–746. doi:10.1103/revmodphys.61.689.

980 [51] C. Freysoldt, B. Grabowski, T. Hickel, J. Neugebauer, G. Kresse, A. Janotti, C. G. V. de Walle, First-principles calculations for point defects in solids, Reviews of Modern Physics 86 (1) (2014) 253–305. doi:10.1103/revmodphys.86.253.

984 [52] J. Coutinho, Density functional modeling of defects and impurities in silicon materials, in: Y. Yoshida, G. Langouche (Eds.), Defects and Impurities in Silicon

986 Materials, Vol. 916 of Lecture Notes in Physics, Springer Japan, Tokyo, 2015,
987 pp. 69–127. doi:10.1007/978-4-431-55800-2_2.

988 [53] C. J. Pickard, F. Mauri, First-principles theory of the EPR g-tensor in
989 solids: defects in quartz, Physical Review Letters 88 (8) (2002) 086403.
990 doi:10.1103/physrevlett.88.086403.

991 [54] V. Ivády, I. A. Abrikosov, A. Gali, First principles calculation of spin-related
992 quantities for point defect qubit research, npj Computational Materials 4 (1).
993 doi:10.1038/s41524-018-0132-5.

994 [55] A. Alkauskas, J. L. Lyons, D. Steiauf, C. G. V. de Walle, First-principles cal-
995 culations of luminescence spectrum line shapes for defects in semiconductors:
996 the example of GaN and ZnO, Physical Review Letters 109 (26) (2012) 267401.
997 doi:10.1103/physrevlett.109.267401.

998 [56] A. Alkauskas, Q. Yan, C. G. V. de Walle, First-principles theory of nonradia-
999 tive carrier capture via multiphonon emission, Physical Review B 90 (7) (2014)
1000 075202. doi:10.1103/physrevb.90.075202.

1001 [57] A. Mattausch, M. Bockstedte, O. Pankratov, Structure and vibrational spec-
1002 tra of carbon clusters in SiC, Physical Review B 70 (23) (2004) 235211.
1003 doi:10.1103/physrevb.70.235211.

1004 [58] S. K. Estreicher, T. M. Gibbons, B. Kang, M. B. Bebek, Phonons and defects
1005 in semiconductors and nanostructures: Phonon trapping, phonon scattering, and
1006 heat flow at heterojunctions, Journal of Applied Physics 115 (1) (2014) 012012.
1007 doi:10.1063/1.4838059.

1008 [59] M.-J. Zheng, N. Swaminathan, D. Morgan, I. Szlufarska, Energy barriers for
1009 point-defect reactions in 3C-SiC, Physical Review B 88 (5) (2013) 054105.
1010 doi:10.1103/physrevb.88.054105.

1011 [60] M. E. Bathen, J. Coutinho, H. M. Ayedh, J. U. Hassan, I. Farkas, S. Öberg, Y. K.
1012 Frodason, B. G. Svensson, L. Vines, Anisotropic and plane-selective migration

Journal Pre-proof

Journal Pre-proof

1013 of the carbon vacancy in SiC: theory and experiment, Physical Review B 100 (1)
1014 (2019) 014103. doi:10.1103/physrevb.100.014103.

1015 [61] J. Coutinho, O. Andersen, L. Dobaczewski, K. B. Nielsen, A. R. Peaker,
1016 R. Jones, S. Öberg, P. R. Briddon, Effect of stress on the energy levels of the
1017 vacancy-oxygen-hydrogen complex in Si, Physical Review B 68 (18) (2003)
1018 184106. doi:10.1103/physrevb.68.184106.

1019 [62] V. Radulović, Y. Yamazaki, Ž. Pastuović, A. Sarbutt, K. Ambrožič, R. Bernat,
1020 Z. Ereš, J. Coutinho, T. Ohshima, I. Capan, L. Snoj, Silicon carbide neutron
1021 detector testing at the JSI TRIGA reactor for enhanced border and port secu-
1022 rity, Nuclear Instruments and Methods in Physics Research Section A: Acceler-
1023 ators, Spectrometers, Detectors and Associated Equipment 972 (2020) 164122.
1024 doi:10.1016/j.nima.2020.164122.

1025 [63] V. Radulović, K. Ambrožič, I. Capan, R. Bernat, Z. Ereš, Željko Pastuović,
1026 A. Sarbutt, T. Ohshima, Y. Yamazaki, T. Makino, J. Coutinho, L. Snoj, Sili-
1027 con carbide neutron detector prototype testing at the JSI TRIGA reactor for en-
1028 hanced border and ports security, in: submitted for presentation at the PHYSOR
1029 2020 conference, Cambridge, UK, 2020.

1030 [64] C. Manfredotti, A. L. Giudice, F. Fasolo, E. Vittone, C. Paolini, F. Fizzotti,
1031 A. Zanini, G. Wagner, C. Lanzieri, SiC detectors for neutron monitoring, Nu-
1032 clear Instruments and Methods in Physics Research Section A: Accelerators,
1033 Spectrometers, Detectors and Associated Equipment 552 (1-2) (2005) 131–137.
1034 doi:10.1016/j.nima.2005.06.018.

1035 [65] I. Capan, T. Brodar, Ž. Pastuović, R. Siegele, T. Ohshima, S. ichiro Sato,
1036 T. Makino, L. Snoj, V. Radulović, J. Coutinho, V. J. B. Torres, K. Demmouche,
1037 Double negatively charged carbon vacancy at the h- and k-sites in 4H-SiC: com-
1038 bined Laplace-DLTS and DFT study, Journal of Applied Physics 123 (16) (2018)
1039 161597. doi:10.1063/1.5011124.

1040 [66] T. Brodar, I. Capan, V. Radulović, L. Snoj, Ž. Pastuović, J. Coutinho,
1041 T. Ohshima, Laplace DLTS study of deep defects created in neutron-irradiated

n-type 4H-SiC, Nuclear Instruments and Methods in Physics Research Section B: Beam Interactions with Materials and Atoms 437 (2018) 27–31. doi:10.1016/j.nimb.2018.10.030.

[67] L. S. Ramsdell, Studies on silicon carbide, American Mineralogist 31 (1-2) (1947) 64–82.

[68] H. Jagodzinski, Polytypism in SiC crystals, Acta Crystallographica 7 (3) (1954) 300. doi:10.1107/s0365110x54000837.

[69] N. W. Ashcroft, N. D. Mermin, Solid state physics, Saunders College Publishing, Fort Worth, 1976.

[70] W. van Haeringen, P. A. Bobbert, W. H. Backes, On the band gap variation in SiC polytypes, physica status solidi (b) 202 (1) (1997) 63–79. doi:10.1002/1521-3951(199707)202:1<63::aid-pssb63>3.0.co;2-e.

[71] J. Dong, A.-B. Chen, Fundamental properties of SiC: crystal structure, bonding energy, band structure, and lattice vibrations, in: Z. C. Feng (Ed.), SiC Power Materials, Vol. 73 of Springer Series in Materials Science, Springer, Berlin, 2004, pp. 63–87. doi:10.1007/978-3-662-09877-6_2.

[72] J. P. Perdew, K. Burke, M. Ernzerhof, Generalized gradient approximation made simple, Physical Review Letters 77 (18) (1996) 3865–3868. doi:10.1103/physrevlett.77.3865.

[73] M. Shishkin, M. Marsman, G. Kresse, Accurate quasiparticle spectra from self-consistent GW calculations with vertex corrections, Physical Review Letters 99 (24) (2007) 246403. doi:10.1103/physrevlett.99.246403.

[74] J. Heyd, G. E. Scuseria, M. Ernzerhof, Hybrid functionals based on a screened Coulomb potential, The Journal of Chemical Physics 118 (18) (2003) 8207–8215. doi:10.1063/1.1564060.

[75] A. V. Krukau, O. A. Vydrov, A. F. Izmaylov, G. E. Scuseria, Influence of the exchange screening parameter on the performance of screened hy-

Journal Pre-proof

Journal Pre-proof

1069 brid functionals, The Journal of Chemical Physics 125 (22) (2006) 224106.
1070 doi:10.1063/1.2404663.

1071 [76] J. Coutinho, V. J. B. Torres, K. Demmouche, S. Öberg, Theory of the carbon va-
1072 cancy in 4H-SiC: crystal field and pseudo-Jahn-Teller effects, Physical Review
1073 B 96 (17) (2017) 174105. doi:10.1103/physrevb.96.174105.

1074 [77] O. Madelung, U. Rössler, M. Schulz (Eds.), Group IV elements, IV-IV and III-V
1075 compounds. Part a - lattice properties, Vol. 41A1α of Landolt-Börnstein - Group
1076 III Condensed Matter, Springer-Verlag, 2001. doi:10.1007/b60136.

1077 [78] O. Madelung (Ed.), Semiconductors, Springer-Verlag, Berlin, 1991.
1078 doi:10.1007/978-3-642-45681-7.

1079 [79] Properties of silicon carbide, in: G. L. Harris (Ed.), EMIS Data Review No. 13,
1080 INSPEC, IEE, London, 1995.

1081 [80] Y. M. Tairov, V. F. Tsvetkov, General principles of growing large-size single
1082 crystals of various silicon carbide polytypes, Journal of Crystal Growth 52
1083 (1981) 146–150. doi:10.1016/0022-0248(81)90184-6.

1084 [81] M. Ito, L. Storasta, H. Tsuchida, Development of 4H-SiC epitaxial growth tech-
1085 nique achieving high growth rate and large-area uniformity, Applied Physics
1086 Express 1 (1) (2008) 015001. doi:10.1143/apex.1.015001.

1087 [82] T. Kimoto, A. Itoh, H. Matsunami, Step-controlled epitaxial growth of
1088 high-quality SiC layers, physica status solidi (b) 202 (1) (1997) 247–262.
1089 doi:10.1002/1521-3951(199707)202:1<247::aid-pssb247>3.0.co;2-q.

1090 [83] A. Itoh, H. Matsunami, Analysis of Schottky barrier heights of metal/SiC
1091 contacts and its possible application to high-voltage rectifying devices,
1092 physica status solidi (a) 162 (1) (1997) 389–408. doi:10.1002/1521-
1093 396x(199707)162:1<389::aid-pssa389>3.0.co;2-x.

1094 [84] A. V. Kuchuk, P. Borowicz, M. Wzorek, M. Borysiewicz, R. Ratajczak, K. Go-
1095 laszewska, E. Kaminska, V. Kladko, A. Piotrowska, Ni-based Ohmic contacts

Journal Pre-proof

1096 to n-type 4H-SiC: the formation mechanism and thermal stability, Advances in
1097 Condensed Matter Physics 2016 (2016) 1–26. doi:10.1155/2016/9273702.

1098 [85] L. M. Porter, R. F. Davis, A critical review of Ohmic and rectifying contacts for
1099 silicon carbide, Materials Science and Engineering: B 34 (2-3) (1995) 83–105.
1100 doi:10.1016/0921-5107(95)01276-1.

1101 [86] I. Capan, T. Brodar, J. Coutinho, T. Ohshima, V. P. Markevich, A. R. Peaker,
1102 Acceptor levels of the carbon vacancy in 4H-SiC: combining Laplace deep level
1103 transient spectroscopy with density functional modeling, Journal of Applied
1104 Physics 124 (24) (2018) 245701. doi:10.1063/1.5063773.

1105 [87] W. Shockley, W. T. Read, Statistics of the recombinations of holes and electrons,
1106 Physical Review 87 (5) (1952) 835–842. doi:10.1103/physrev.87.835.

1107 [88] T. Kimoto, A. Itoh, H. Matsunami, S. Sridhara, L. L. Clemen, R. P. Devaty, W. J.
1108 Choyke, T. Dalibor, C. Peppermüller, G. Pensl, Nitrogen donors and deep levels
1109 in high-quality 4H-SiC epilayers grown by chemical vapor deposition, Applied
1110 Physics Letters 67 (19) (1995) 2833–2835. doi:10.1063/1.114800.

1111 [89] C. Hemmingsson, N. T. Son, O. Kordina, J. P. Bergman, E. Janzén, J. L. Lind-
1112 ström, S. Savage, N. Nordell, Deep level defects in electron-irradiated 4H-
1113 SiC epitaxial layers, Journal of Applied Physics 81 (9) (1997) 6155–6159.
1114 doi:10.1063/1.364397.

1115 [90] G. Alfieri, E. V. Monakhov, B. G. Svensson, M. K. Linnarsson, Annealing be-
1116 havior between room temperature and 2000 °C of deep level defects in electron-
1117 irradiated n-type 4H silicon carbide, Journal of Applied Physics 98 (4) (2005)
1118 043518. doi:10.1063/1.2009816.

1119 [91] C. G. Hemmingsson, N. T. Son, A. Ellison, J. Zhang, E. Janzén, Negative-*U* cen-
1120 ters in 4H silicon carbide, Physical Review B 58 (16) (1998) R10119–R10122.
1121 doi:10.1103/physrevb.58.r10119.

1122 [92] N. T. Son, X. T. Trinh, L. S. Løvlie, B. G. Svensson, K. Kawahara, J. Suda,
1123 T. Kimoto, T. Umeda, J. Isoya, T. Makino, T. Ohshima, E. Janzén, Negative-*U*

Journal Pre-proof

Journal Pre-proof

1124 system of carbon vacancy in 4H-SiC, Physical Review Letters 109 (18) (2012)
1125 187603. doi:10.1103/physrevlett.109.187603.

1126 [93] V. Markevich, L. Murin, T. Sekiguchi, M. Suezawa, Emission and capture
1127 kinetics for a hydrogen-related negative-U center in silicon: evidence for
1128 metastable neutral charge state, Materials Science Forum 258-263 (1997) 217–
1129 222. doi:10.4028/www.scientific.net/msf.258-263.217.

1130 [94] T. Hornos, A. Gali, B. G. Svensson, Large-scale electronic structure calcu-
1131 lations of vacancies in 4H-SiC using the Heyd-Scuseria-Ernzerhof screened
1132 hybrid density functional, Materials Science Forum 679-680 (2011) 261–264.
1133 doi:10.4028/www.scientific.net/msf.679-680.261.

1134 [95] H. M. Ayedh, V. Bobal, R. Nipoti, A. Hallén, B. G. Svensson, Formation of car-
1135 bon vacancy in 4H silicon carbide during high-temperature processing, Journal
1136 of Applied Physics 115 (1) (2014) 012005. doi:10.1063/1.4837996.

1137 [96] S. Sciortino, F. Hartjes, S. Lagomarsino, F. Nava, M. Brianzi, V. Cindro,
1138 C. Lanzieri, M. Moll, P. Vanni, Effect of heavy proton and neutron irradia-
1139 tions on epitaxial 4H-SiC Schottky diodes, Nuclear Instruments and Methods in
1140 Physics Research Section A: Accelerators, Spectrometers, Detectors and Asso-
1141 ciated Equipment 552 (1-2) (2005) 138–145. doi:10.1016/j.nima.2005.06.017.

1142 [97] F. H. Ruddy, A. R. Dulloo, J. G. Seidel, F. W. Hantz, L. R. Grobmyer, Nuclear
1143 reactor power monitoring using silicon carbide semiconductor radiation detec-
1144 tors, Nuclear Technology 140 (2) (2002) 198–208. doi:10.13182/nt02-a3333.

1145 [98] L.-Y. Liu, X. Ouyang, J.-L. Ruan, S. Bai, X.-P. Ouyang, Performance com-
1146 parison between SiC and Si neutron detectors in deuterium-tritium fusion neu-
1147 tron irradiation, IEEE Transactions on Nuclear Science 66 (4) (2019) 737–741.
1148 doi:10.1109/tns.2019.2901797.

1149 [99] E. V. Kalinina, G. F. Kholuyanov, D. V. Davydov, A. M. Strel'chuk, A. Hal-
1150 lén, A. O. Konstantinov, V. V. Luchinin, A. Y. Nikiforov, Effect of irra-
1151 diation with fast neutrons on electrical characteristics of devices based on

Journal Pre-proof

Journal Pre-proof

1152 CVD 4H-SiC epitaxial layers, Semiconductors 37 (10) (2003) 1229–1233.
1153 doi:10.1134/1.1619523.

1154 [100] E. Omotoso, W. E. Meyer, F. D. Auret, A. T. Paradzah, M. J. Legodi, Electrical
1155 characterization of deep levels created by bombarding nitrogen-doped 4H-SiC
1156 with alpha-particle irradiation, Nuclear Instruments and Methods in Physics Re-
1157 search Section B: Beam Interactions with Materials and Atoms 371 (2016) 312–
1158 316. doi:10.1016/j.nimb.2015.09.084.

1159 [101] L. Storasta, J. P. Bergman, E. Janzén, A. Henry, J. Lu, Deep levels created by
1160 low energy electron irradiation in 4H-SiC, Journal of Applied Physics 96 (9)
1161 (2004) 4909–4915. doi:10.1063/1.1778819.

1162 [102] N. Iwamoto, B. C. Johnson, N. Hoshino, M. Ito, H. Tsuchida, K. Kojima,
1163 T. Ohshima, Defect-induced performance degradation of 4H-SiC Schottky bar-
1164 rier diode particle detectors, Journal of Applied Physics 113 (14) (2013) 143714.
1165 doi:10.1063/1.4801797.

1166 [103] K. Kawahara, X. T. Trinh, N. T. Son, E. Janzén, J. Suda, T. Kimoto, Inves-
1167 tigation on origin of $Z_{1/2}$ center in SiC by deep level transient spectroscopy
1168 and electron paramagnetic resonance, Applied Physics Letters 102 (11) (2013)
1169 112106. doi:10.1063/1.4796141.

1170 [104] M. L. David, G. Alfieri, E. M. Monakhov, A. Hallén, C. Blanchard, B. G. Svens-
1171 son, J. F. Barbot, Electrically active defects in irradiated 4H-SiC, Journal of Ap-
1172 plied Physics 95 (9) (2004) 4728–4733. doi:10.1063/1.1689731.

1173 [105] A. Castaldini, A. Cavallini, L. Rigutti, F. Nava, Low temperature annealing of
1174 electron irradiation induced defects in 4H-SiC, Applied Physics Letters 85 (17)
1175 (2004) 3780–3782. doi:10.1063/1.1810627.

1176 [106] A. Castaldini, A. Cavallini, L. Rigutti, F. Nava, S. Ferrero, F. Giorgis, Deep
1177 levels by proton and electron irradiation in 4H-SiC, Journal of Applied Physics
1178 98 (5) (2005) 053706. doi:10.1063/1.2014941.

Journal Pre-proof

1179 [107] A. T. Paradzah, F. D. Auret, M. J. Legodi, E. Omotoso, M. Diale, Elec-
1180 trical characterization of 5.4 MeV alpha-particle irradiated 4H-SiC with low
1181 doping density, Nuclear Instruments and Methods in Physics Research Sec-
1182 tion B: Beam Interactions with Materials and Atoms 358 (2015) 112–116.
1183 doi:10.1016/j.nimb.2015.06.006.

1184 [108] M. E. Bathen, A. Galeckas, J. Müting, H. M. Ayedh, U. Grossner, J. Coutinho,
1185 Y. K. Frodason, L. Vines, Electrical charge state identification and control for
1186 the silicon vacancy in 4H-SiC, npj Quantum Information 5 (1) (2019) 111.
1187 doi:10.1038/s41534-019-0227-y.

1188 [109] G. Alfieri, A. Mihaila, Isothermal annealing study of the EH_1 and EH_3 levels in
1189 n-type 4H-SiC, Journal of Physics: Condensed Matter 32 (46) (2020) 465703.
1190 doi:10.1088/1361-648x/abaeaf.

1191 [110] L. Snoj, A. Trkov, R. Jaćimović, P. Rogan, G. Žerovnik, M. Ravnik, Analysis of
1192 neutron flux distribution for the validation of computational methods for the op-
1193 timization of research reactor utilization, Applied Radiation and Isotopes 69 (1)
1194 (2011) 136–141. doi:10.1016/j.apradiso.2010.08.019.

1195 [111] L. Snoj, G. Žerovnik, A. Trkov, Computational analysis of irradiation facilities
1196 at the JSI TRIGA reactor, Applied Radiation and Isotopes 70 (3) (2012) 483–
1197 488. doi:10.1016/j.apradiso.2011.11.042.

1198 [112] K. Ambrožič, G. Žerovnik, L. Snoj, Computational analysis of the dose rates
1199 at JSI TRIGA reactor irradiation facilities, Applied Radiation and Isotopes 130
1200 (2017) 140–152. doi:10.1016/j.apradiso.2017.09.022.

1201 [113] Ž. Štancar, L. Barbot, C. Destouches, D. Fourmentel, J.-F. Villard, L. Snoj, Com-
1202 putational validation of the fission rate distribution experimental benchmark at
1203 the JSI TRIGA Mark II research reactor using the Monte Carlo method, Annals
1204 of Nuclear Energy 112 (2018) 94–108. doi:10.1016/j.anucene.2017.09.039.

1205 [114] I. Capan, T. Brodar, Y. Yamazaki, Y. Oki, T. Ohshima, Y. Chiba, Y. Hijikata,
1206 L. Snoj, V. Radulović, Influence of neutron radiation on majority and minority

Journal Pre-proof

1207 carrier traps in n-type 4H-SiC, Nuclear Instruments and Methods in Physics
1208 Research Section B: Beam Interactions with Materials and Atoms 478 (2020)
1209 224–228. doi:10.1016/j.nimb.2020.07.005.

1210 [115] V. Radulović, K. Ambrožič, L. Snoj, I. Capan, T. Brodar, Z. Ereš, Željko Pas-
1211 tuović, A. Sarbutt, T. Ohshima, Y. Yamazaki, J. Coutinho, E-SiCure collabora-
1212 tion project: silicon carbide material studies and detector prototype testing at
1213 the JSI TRIGA reactor, in: T. Žagar (Ed.), Proceedings of the 27th International
1214 Conference Nuclear Energy for New Europe (NENE 2018), Ljubljana, Slovenia,
1215 2018, p. 702.

1216 [116] R. Capote, K. I. Zolotarev, V. G. Pronyaev, A. Trkov, Updating and extending
1217 the IRDF-2002 dosimetry library, Journal of ASTM International 9 (4) (2012)
1218 104119. doi:10.1520/jai104119.

1219 [117] J. T. Goorley, M. James, T. Booth, F. Brown, J. Bull, L. J. Cox, J. Durkee,
1220 J. Elson, M. Fensin, R. A. Forster, J. Hendricks, H. G. Hughes, R. Johns,
1221 B. Kiedrowski, R. Martz, S. Mashnik, G. McKinney, D. Pelowitz, R. Prael,
1222 J. Sweezy, L. Waters, T. Wilcox, T. Zukaitis, Initial MCNP6 release overview
1223 - MCNP6 version 1.0, techreport LA-UR-13- 22934, Los Alamos National
1224 Laboratory, US (2013).
1225 URL https://laws.lanl.gov/vhosts/mcnp.lanl.gov/pdf_files/la-ur-13-22934.pdf

1226 [118] M. B. Chadwick, M. Herman, P. Obložinský, M. E. Dunn, Y. Danon, A. C.
1227 Kahler, D. L. Smith, B. Pritychenko, G. Arbanas, R. Arcilla, R. Brewer, D. A.
1228 Brown, R. Capote, A. D. Carlson, Y. S. Cho, H. Derrien, K. Guber, G. M.
1229 Hale, S. Hoblit, S. Holloway, T. D. Johnson, T. Kawano, B. C. Kiedrowski,
1230 H. Kim, S. Kunieda, N. M. Larson, L. Leal, J. P. Lestone, R. C. Little, E. A. Mc-
1231 Cutchan, R. E. MacFarlane, M. MacInnes, C. M. Mattoon, R. D. McKnight,
1232 S. F. Mughabghab, G. P. A. Nobre, G. Palmiotti, A. Palumbo, M. T. Pigni,
1233 V. G. Pronyaev, R. O. Sayer, A. A. Sonzogni, N. C. Summers, P. Talou, I. J.
1234 Thompson, A. Trkov, R. L. Vogt, S. C. van der Marck, A. Wallner, M. C. White,
1235 D. Wiarda, P. G. Young, ENDF/B-VII.1 Nuclear data for science and technol-

Journal Pre-proof

1236 ogy: cross sections, covariances, fission product yields and decay data, Nuclear
1237 Data Sheets 112 (12) (2011) 2887–2996. doi:10.1016/j.nds.2011.11.002.

1238 [119] R. Jeraj, M. Ravnik, TRIGA mark II reactor: U(20)-zirconium hydride fuel
1239 rods in water with graphite reflector, IEU-COMP-THERM-003, in: Interna-
1240 tional Handbook of Evaluated Criticality Safety Benchmark Experiments, no.
1241 NEA/NSC/DOC(95)03, OECD-NEA, Paris, 2010.

1242 [120] International handbook of evaluated criticality safety benchmark experi-
1243 ments, techreport NEA/NSC/DOC(95)03/I-IX, Organisation for Economic Co-
1244 operation and Development-Nuclear Energy Agency (OECD-NEA) (Sep. 2010).

1245 [121] V. Radulović, A. Kolšek, A. Jazbec, Žiga Štancar, A. Trkov, L. Snoj, Character-
1246 ization of the ex-core irradiation facilities of the JSI TRIGA Mark II reactor, in:
1247 T. Žagar (Ed.), Proceedings of the 21st International Conference Nuclear Energy
1248 for New Europe (NENE 2012), Ljubljana, Slovenia, 2012, p. 1004.

1249 [122] I. Mandic, V. Cindro, G. Kramberger, E. S. Kristof, M. Mikuz, D. Vrtacnik,
1250 M. Ullan, F. Anghinolfi, Bulk damage in DMILL npn bipolar transistors caused
1251 by thermal neutrons versus protons and fast neutrons, IEEE Transactions on
1252 Nuclear Science 51 (4) (2004) 1752–1758. doi:10.1109/tns.2004.832927.

1253 [123] I. Mandic, V. Cindro, A. Gorisek, G. Kramberger, M. Mikuz, Online integrat-
1254 ing radiation monitoring system for the ATLAS detector at the large hadron
1255 collider, IEEE Transactions on Nuclear Science 54 (4) (2007) 1143–1150.
1256 doi:10.1109/tns.2007.895120.

1257 [124] G. V. Gorshkov, V. A. Zyabkin, O. S. Tsvetkov, The neutron background
1258 at the surface of the earth, Soviet Atomic Energy 17 (6) (1964) 1256–1260.
1259 doi:10.1007/bf01122773.

Declaration of interests

☒ The authors declare that they have no known competing financial interests or personal relationships that could have appeared to influence the work reported in this paper.

☐The authors declare the following financial interests/personal relationships which may be considered as potential competing interests:

Journal Pre-proof